ADVANCED ENERGY MATERIALS
www.advenergymat.de

Earth-Abundant Na-Mg-Fe-Mn-O Cathode with Reversible Hybrid Anionic and Cationic Redox

Yaoshen Niu, Zilin Hu, Bo Zhang, Dongdong Xiao, Huican Mao, Lin Zhou, Feixiang Ding, Yuan Liu, Yang Yang, Juping Xu, Wen Yin, Nian Zhang, Zhiwei Li, Xiqian Yu, Hao Hu, Yaxiang Lu, Xiaohui Rong,* Ju Li,* and Yong-Sheng Hu**

Na-ion batteries (NIBs) are promising for grid-scale energy storage applications. However, the lack of Co, Ni-free cathode materials has made them less cost-effective. In this work, Mg^{2+} is successfully utilized to activate the oxygen redox reaction in earth-abundant Fe/Mn-based layered cathodes to achieve reversible hybrid anionic and cationic redox capacities. A high first charge capacity of ≈210 mAh g^{-1} with balanced charge–discharge efficiency is achieved without O-loss, showing a promising energy cost of \$2.02 kWh^{-1}. Full cell against hard carbon anode without pre-sodiation shows energy density exceeding ≈280 Wh kg^{-1} with a decent capacity retention of 85.6% after 100 cycles. A comprehensive analysis of the charge compensation mechanisms and structural evolution is conducted. Voltage and capacity loss resulting from partially reversible Fe^{3+} migration to the Na layer is confirmed, shedding light on further improvements for low-cost NIB cathodes in application scenarios.

1. Introduction

Renewable electricity is increasingly important, but intermittency and geographic dispersion create inherent limitations that require the development of large-scale electric energy storage systems. The rapid growth of portable devices and electric vehicles in recent years has exacerbated the scarcity of lithium sources. Na-ion batteries (NIBs), an electrochemical analog to lithium-ion batteries (LIBs), are attractive due to the abundance of Na. As such, NIBs may offer an excellent complement to LIBs in grid-scale energy storage applications, where energy density is less critical.[1,2] However, the lack of suitable and cost-effective cathode materials with high capacity and excellent cycle stability has made it challenging for practical use. We note that even though the cost of Na is less than one-tenth that of Li, the per-molar cost of transition metals Co is 4×, and Ni is 0.7×, that of Li. Therefore, NIBs that use a significant fraction of Co, Ni will greatly negate their economic competitiveness.

Layered cathode materials (Na_xTMO_2; TM = transition metal ions) are an attractive alternative to a wide range of materials due

Y. Niu, H. Hu
Frontier Institute of Science and Technology
Xi'an Jiaotong University
Xi'an 710049, P. R. China
Y. Niu, Z. Hu, D. Xiao, H. Mao, L. Zhou, F. Ding, Y. Liu, Y. Yang, X. Yu, Y. Lu, X. Rong, Y.-S. Hu
Key Laboratory for Renewable Energy
Beijing Key Laboratory for New Energy Materials and Devices
Beijing National Laboratory for Condensed Matter Physics
Institute of Physics
Chinese Academy of Sciences
School of Physical Sciences
University of Chinese Academy of Sciences
Beijing 100190, P. R. China
E-mail: dongdongxiao@iphy.ac.cn; rong@iphy.ac.cn; yshu@iphy.ac.cn

The ORCID identification number(s) for the author(s) of this article can be found under https://doi.org/10.1002/aenm.202300746

DOI: 10.1002/aenm.202300746

B. Zhang, Z. Li
Key Lab for Magnetism and Magnetic Materials of the Ministry of Education
Lanzhou University
Lanzhou 730000, P. R. China
J. Xu, W. Yin
Spallation Neutron Source Science Center
Dongguan 523803, P. R. China
N. Zhang
State Key Laboratory of Functional Materials for Informatics
Shanghai Institute of Microsystem and Information Technology
Chinese Academy of Sciences
Shanghai 200050, P. R. China
J. Li
Department of Nuclear Science and Engineering and Department of Materials Science and Engineering
MIT
Cambridge, MA 02139, USA
E-mail: liju@mit.edu

to their low cost and ease of synthesis. Particularly, Na_xTMO_2 based on Fe and Mn garnered considerable research interest due to the abundance and low cost of Fe and Mn, including P2- and O3-types.[3–5] According to the nomenclature proposed by Delmas et al.,[6] symbols of O or P denote the octahedral or prismatic environment for Na sites, and symbols of 2 or 3 indicate the minimum number of transition metal layers in the repeating cell unit. However, the low charge capacity of traditional Fe-Mn-based oxide cathodes based solely on TM-redox reactions and the unstable structure due to the presence of Mn^{3+} with Jahn–Teller effect have hindered their practical implementation in NIBs.[4,7–9] Several proposals have been made to increase the practical capacity, such as Cu-substitution, which has enhanced electrochemical performance but still shows inadequate capacity.[10] Hence, activating oxygen redox has been regarded as a key strategy to further increase the capacity of cathode materials.[11–13] It has been shown that in comparison to lithium-rich materials with the Li-O-Li configuration, layered NIB cathode materials have a greater variety of Na-O-*X* configurations (*X* = Li, Na, Mg, vacancies, Zn) capable of forming the unhybridized O 2p state, which is a critical prerequisite for activating oxygen anionic redox.[14–16]

NIB cathode materials are designed primarily to increase energy density and cycle stability. It would be excellent if the ingredients used were environmentally and economically acceptable. Figure S1 (Supporting Information) compares elemental abundance in the Earth's crust for elements used in electrode materials for rechargeable NIBs.[17] Considering the charge compensation mechanisms discussed above, we utilize Mg^{2+} to trigger the oxygen redox reaction in Fe/Mn-based layered cathodes to achieve hybrid anionic and cationic redox (HACR) reactions simultaneously to provide charge compensation. The incorporation of divalent Mg pushes up the average valence of Fe/Mn, and meanwhile reduces the content of Fe to a certain extent to mitigate the effect of Fe migration on structural deterioration. Besides, the activated anion-redox reaction provides charge compensation to cover the loss of TM content. Moreover, the doping of Mg can effectively prevent the O_2 loss from the lattice. [18] Herein, we report the successful doping of Mg^{2+} into the TM layers of a typical O3-type $NaFe_{0.5}Mn_{0.5}O_2$ (NaFM) cathode, which gives a composition of $Na_{0.83}Mg_{0.33}Fe_{0.17}Mn_{0.50}O_2$ (NaMFM). The iron, manganese, and oxygen in this configuration undergo synergistically reversible HACR, contributing to a high charge capacity of 207 mAh g^{-1} and good cycling performance in half cells. Moreover, comprehensive analysis with neutron powder diffraction (NPD), *operando* X-ray diffraction (XRD), ex situ neutron pair distribution function (nPDF), hard and soft X-ray absorption spectra (hXAS and sXAS), ^{57}Fe-Mössbauer spectroscopy (Fe-MS), and scanning transmission microscope (STEM) have revealed charge–discharge mechanisms and structural changes in O3-$Na_{0.83}Mg_{0.33}Fe_{0.17}Mn_{0.50}O_2$ samples.

2. Results and Discussion

2.1. Crystal Structure

The O3-type $NaFe_{0.5}Mn_{0.5}O_2$ and O3-type $Na_{0.83}Mg_{0.33}Fe_{0.17}Mn_{0.50}O_2$ samples were synthesized by a simple solid-state reaction. Detailed synthesis conditions are described in the Supporting Information. The chemical compositions of samples NaMFM and NaFM were analyzed by inductively coupled plasma (ICP), and the results are listed in Table S1 (Supporting Information). The actual molar ratio of Na, Mg, Fe, and Mn elements in NaMFM was 0.82(1):0.35(1):0.17(1):0.5, and the actual molar ratio of Na, Fe, and Mn elements in NaFM was 0.98(1):0.51(1):0.5, consistent with the designed compositions. The crystal structure of the NaMFM and NaFM samples was analyzed using XRD with Rietveld refinement, as shown in Figure S2 and Table S2 (Supporting Information). In addition, the crystal structure of the NaMFM sample was confirmed through NPD and nPDF measurements, which were also refined using the Rietveld method, as depicted in **Figure 1**a,b. The XRD and NPD patterns are devoid of any discernible impurity diffraction peaks, short-range ordered superstructure peaks, and peak asymmetric broadening, as shown in Figure S2 (Supporting Information) and Figure 1a, indicating that NaMFM sample had a high-quality long-range ordering without stacking faults. Furthermore, both XRD and NPD patterns can be well indexed by an O3-type $NaFeO_2$ structure using a space group of *R-3m* (inset in Figure 1a). The refined lattice parameters of NaMFM were $a = b = 2.94337(16)$ Å and $c = 16.3047(9)$ Å according to the NPD Rietveld refinement. Figure 1b shows the nPDF result of pristine NaMFM, the O3 structure was used as the model for the refinement, and the fitting yields an R_w of 25.266%, listed in Table S3 (Supporting Information). It should be noted that the fitting results below 2.5 Å are not ideal. This may be attributed to the opposing contribution of Mn and Fe to the pattern, which cancels each other out due to the negative neutron scattering length of Mn ions (−3.73 fm) and the possible differences in local bond lengths between the two cations caused by differences in ionic size. Therefore, it is likely that the peak at 2.07 Å primarily corresponds to the Fe/Mg–O bond, while the Mn–O pair is located at 1.87 Å with a negative amplitude. Such phenomena can be seen in other FeMn-containing cathodes.[19,20] Our NPD and nPDF refinement results did not show any evidence for the presence of TM layer vacancies or Mg residing in the Na layer. The crystal structure of the O3-NaMFM was further characterized using atomic resolution STEM imaging, as seen in Figure S3a,b (Supporting Information), which includes both high-angle annular dark-field (HAADF) and annular bright-field (ABF) STEM images. For the HAADF-STEM image shown in Figure S3a (Supporting Information), the bright spots, due to the Z contrast, represent the transition metal ions viewed from the [100] axis, showing no obvious stacking faults or cation migration; the distance of the adjacent layer in the HAADF-STEM image is measured to be ≈0.54 nm, which corresponds to the interslab distance from the NPD refinement. The faint bright contrast between the octahedral TMO_2 slabs in the ABF-STEM image (Figure S3b, Supporting Information) represents the Na and O columns, which is consistent with the O3-type structure as demonstrated in the Figure 1a inset. Moreover, we conducted atom-scale EDS mapping (Figure S4, Supporting Information) and the results demonstrate that the Mg, Fe, and Mn elements are distributed uniformly in the TM layer. As seen in Figure 1c, field-emission scanning electron microscopy (FESEM) reveals that NaMFM has a typical plate-like shape with a distribution of sizes in the range of 2–4 μm. In addition, the X-ray energy dispersive spectroscopy (EDS) mapping (Figure 1d) result demonstrates that Na, Mg, Fe,

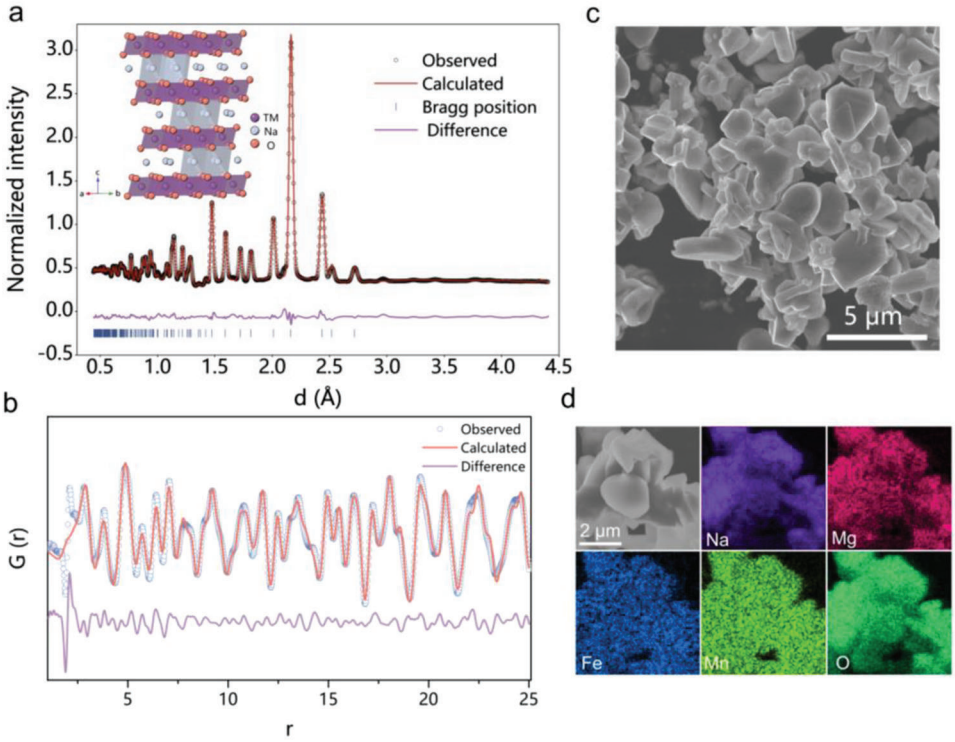

Figure 1. Structural, morphological characterization of O3-NaMFM. a) Refined NPD pattern of O3-NaMFM. Inset: the schematic illustration of the crystal structure of NaMFM. b) nPDF pattern and Rietveld refinement profile. c) SEM image of NaMFM. d) EDS mappings of Na, Mg, Fe, Mn, and O elements.

Mn, and O are distributed uniformly throughout the plate-like particle.

2.2. Electrochemical Performance

The electrochemical performance of the designed NaMFM and NaFM as positive electrode materials for Na-ion batteries was evaluated against Na metal anodes with a liquid electrolyte of 1.0 M $NaClO_4$ in propylene carbonate (PC) and 2 wt% of fluoroethylene carbonate (FEC) in coin cells. **Figure 2**a and Figure S5a (Supporting Information) show the typical charge and discharge profiles of NaMFM and NaFM at 10 mA g^{-1}. In comparison to NaFM phase, the voltage curve shape of NaMFM during the first charge is quite different. The NaFM has a two-step slope corresponding to Mn^{3+}/Mn^{4+} and Fe^{3+}/Fe^{4+}, whereas the NaMFM exhibits a slope accompanied by a well-defined voltage plateau attributed to Fe^{3+}/Fe^{4+} and oxygen redox, consistent with the CV curves (Figure S6, Supporting Information), thus proving the anion-redox activation provided by axial Na-O-Mg configurations that elevate the orbital energy of those particular O *2p* orbitals. As shown in Figure S5a (Supporting Information), voltage hysteresis at the beginning of discharge may indicate the degree of cation migration during the charging process.[21–23] Compared to NaFM, NaMFM exhibits a lower level of hysteresis, which may explain its better cycling performance (Figure S5b, Supporting Information). NaFM delivers ≈190 mAh g^{-1} of initial charge capacity and ≈180 mAh g^{-1} of discharge capacity between 1.5 and 4.3 V. In comparison with the NaFM, the NaMFM clearly shows a better performance. The initial charge capacity reaches ≈210 mAh g^{-1} and the discharge capacity reaches ≈220 mAh g^{-1} under the same experimental conditions. Note that the theoretical capacity based on a single-electron redox process of a Fe^{3+}/Fe^{4+} couple is ≈45 mAh g^{-1}, so the excess capacity during the initial charge process may be attributed to either oxygen redox or electrolyte decomposition, according to earlier reports and the charge compensation mechanism that will be discussed later.[24,25] The subsequent cycle capacity loss may result from the formation of SEI or electrolyte decomposition.[26] The galvanostatic curves of NaMFM for the first cycle in various voltage ranges (Figure S7, Supporting Information) show that as the upper cutoff voltage decreases, the polarization between the charge and discharge processes diminishes, indicating sluggish kinetics in the high voltage area, which is in accordance with the tendency observed in the GITT curve (Figure S8a, Supporting Information). Such a phenomenon has also been observed in many cathode materials with oxygen redox and cation migration.[16,27,28] The cycle performances of NaMFM in various voltage ranges are shown in Figure 2b. For the NaMFM, the discharge capacity increases as per the cutoff voltage: from ≈160 mAh g^{-1} (2.3–4.1 V) to ≈200 mAh g^{-1} (2.0–4.2 V) and finally to ≈220 mAh g^{-1} (1.5–4.3 V). After 50 cycles, experiments conducted in the 2.3–4.1 and 2.0–4.2 V voltage ranges demonstrate good capacity retention of 70% and 69%, respectively. Nevertheless, raising the cutoff voltage to 4.3 V results in poor capacity retention of 61%, which is still much higher than that of NaFM

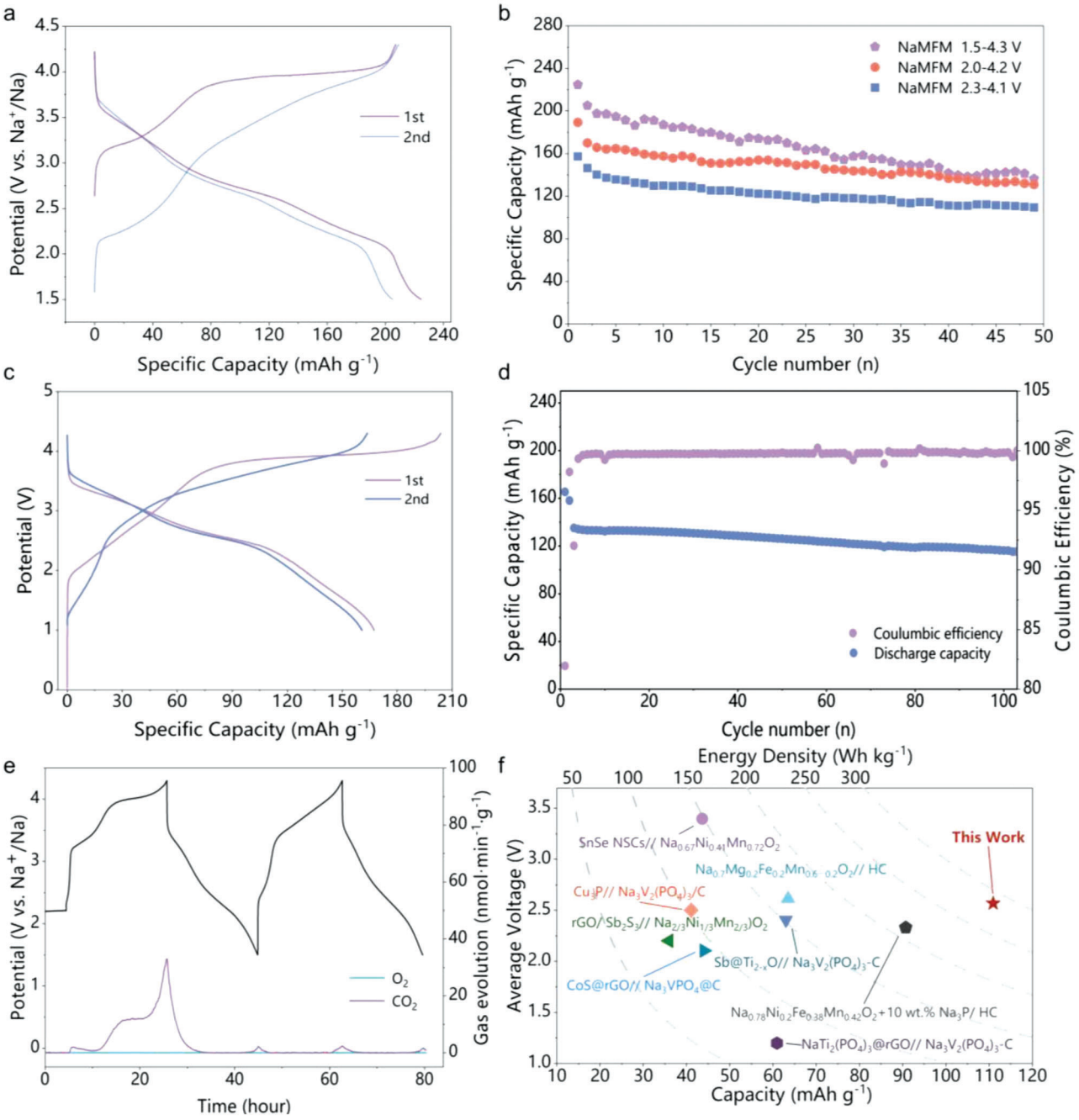

Figure 2. Electrochemical performance of O3-NaMFM. a) Galvanostatic charge and discharge profiles of the Na/NMFM at 10 mA g^{-1} between 1.5 and 4.3 V. b) Comparison of galvanostatic cycling performance between different cycling window at 10 mA g^{-1}. c) Galvanostatic charge–discharge curves of NaMFM/hard carbon full cell at 10 mA g^{-1}. d) Cycle performance of NaMFM// hard carbon full cell at 50 mA g^{-1}, the full cell was precycled at 10 mA g^{-1}. e) Gas loss of NaMFM during electrochemical (de)sodiation. In situ DEMS data collected during the first two cycles of NaMFM at 10 mA g^{-1}. The top panel shows the electrochemical response of the cell, and the bottom panel shows the O_2 and CO_2 gases evolved as a function of time. f) Comparison of the energy density between NaMFM// hard carbon full cell and other reported full cell systems for Na-ion batteries, which have been drawn based on the total mass of the active materials both in the cathode and the anode.

(45.6%) at the 50th cycle (Figure S5b, Supporting Information). Multiple phase transitions and Fe migration may be to blame for NaFM's poor cycling performance.[29–32] The rate capability of NaMFM in the optimized voltage window 2.0–4.2 V is shown in Figure S8b (Supporting Information), in which the NaMFM delivers ≈60% of the reversible capacity at 200 mA g^{-1}. The feasibility of NaMFM as a cathode material is further demonstrated in full cells against hard-carbon anode without any pre-sodiation (Figure 2c). The hard carbon anode was evaluated first in a half-cell, and the charge–discharge curve is shown in Figure S9

(Supporting Information). The full cell delivers a high specific capacity of ≈170 mAh g^{-1} based on the mass of the positive electrode at 10 mA g^{-1} and an average potential of ≈2.6 V. Surprisingly, the full cell exhibits much better cycling performance with a capacity retention of 85.6% after 100 cycles (Figure 2d). It is due to the formation of a relatively stable SEI layer on HC in the full-cell system rather than the repeated formation and decomposition of the SEI layer on the Na anode in half cell.[33]

To further check whether oxygen is lost from the lattice, differential electrochemical mass spectrometry (DEMS) was conducted during the first two cycles. The result of the DEMS measurement is presented in Figure 2e, O_2 gas is not detected upon charging at 4.3 V as only CO_2 was observed, corresponding to previous reports.[34] Considering that we cannot accurately characterize whether Mg migration occurs during the charging process in this study, we can only speculate that this may be due to one of the following reasons: In the first scenario, Mg does not undergo migration, and the presence of the immobile Mg^{2+} prevents the occurrence of underbonded oxidized oxygen, defined as oxygen with less than three cation nearest neighbors, thus suppressing the oxygen loss.[35] In the second scenario, Mg migration does occur, leading to the generation of the O_2 molecules, which are physically trapped in voids within the bulk of the particles formed by in-plane TM migration.[18,36] The detected CO_2 gas is mainly associated with the decomposition of residual carbonates[37] on the material surface and/or from electrolyte oxidation when charged to the high voltage range beyond 3.5 V. In addition, a trace amount CO_2 is detected during the second charging, which indicates that a stable cathode–electrolyte interface protective film has been formed after the 1st cycle. In conclusion, irreversible oxygen loss cannot be detected, indicating that there is no O loss from the NaMFM lattice and Mg^{2+} ions play a stabilizing role in enabling the reversible oxygen redox reactions.

Figure S10 (Supporting Information) summarizes the discharge voltage as a function of specific capacity for the recently reported cathode materials for NIBs. A higher discharge voltage as well as a higher specific capacity are necessary to achieve excellent energy density. The present work shows an impressive cathode-specific energy density of 607.5 Wh kg^{-1} (specific capacity of 225 mAh g^{-1} with an operating voltage of 2.7 V), which holds a unique position among cathode materials for NIBs. Further, the energy cost calculated based on the data in Table S5 (Supporting Information) is 2.02 \$ kWh^{-1}, thus indicating a promising future for this material. In addition, Figure 2f calculates the maximal energy density of the full cell to be 280.3 Wh kg^{-1} (derived from the mass of the active materials in the cathode and anode), which is superior compared to the previous reports.[24,38–45] The results demonstrate that the O3-NaMFM electrode is both feasible and promising for the development of sustainable energy storage systems.

2.3. Charge Compensation Mechanism

To understand the role played by Fe, Mn, and O in the different electrochemical processes, we measured NaMFM samples with different electrochemical states by several ex situ spectroscopic techniques. Ex situ hXAS spectra were collected at the K-edge of Fe and Mn to investigate valence variation and local structure evolution, and the ex situ sXAS at the Fe, Mn $L_{2,3}$-edge and the O K-edge was applied to ascertain the change of the electronic structure of the TM 3*d* and O 2*p* at various states of Na (de)intercalation and to understand the charge compensation mechanism.

Figure 3b,c shows the normalized X-ray absorption near edge structure (XANES) spectra of Fe and Mn K-edges at different charge and discharge states. The Fe K-edge shifts toward higher energy range from the initial state to 3.8 and 4.3 V, suggesting that the valence of Fe changes from the initial +3 to a higher oxidation state. In contrast, the Mn K-edge shows a very slight change in the shape of the absorption peak from 3.8 to 4.3 V, which cannot be assigned to a change in oxidation state but rather to a distortion of the Mn local environment during the Na^+ (de)intercalation process,[46] suggesting that the oxidization of Fe-ions is mainly responsible for the charge compensation during the first charge. However, the total specific capacity in the initial charge processes up to 4.3 V is ≈210 mAh g^{-1} (Figure 2a), which is much higher than the total contribution from Fe^{3+}/Fe^{4+} (48 mAh g^{-1}), suggesting that the extra capacity is provided by the redox reaction on oxygen anions, to be further discussed later. The Fe K-edge shifts are highly reversible upon discharge, while the Mn K-edge shifts to lower energy, even lower than that of the fresh electrode, on discharge to 1.5 V, which demonstrates that Mn is reduced to a lower valence state at the end of the discharge process.

The sXAS data at the Fe, Mn $L_{2,3}$-edge were collected using the total electron yield (TEY) mode. As shown in Figure S11 (Supporting Information), all spectra displayed two peaks in different regions, the low energy range (metal L_3-edge) and the high energy range (metal L_2-edge), as a result of the core-hole spin-orbital-coupling split.[47] The most identifiable states are in the low energy region, and the splitting of the peaks could be ascribed to the TM *2p-3d* electrostatic interaction and crystal field effect.[48] The intensity ratios of the double-peak features in the TM-L_3 regions (A and B) have a negative relation with the oxidation state of TM. After charging the NaMFM electrode to 4.3 V, there was no distinct change in the Mn L-edge sXAS, suggesting that the Mn ions maintain their Mn^{4+} states upon Na^+ deintercalation. However, the peaks of Mn L_3-edge shift to a lower energy area after discharge, which demonstrates the reduction of Mn^{4+} below 3.0 V. The new feature of the spectrum between the 640.7 and 643.3 eV spikes of the Mn^{4+} ion reflects the presence of the Mn^{3+} ion, and the peak around 641 eV originated from Mn^{2+}, and this could be attributed to the heterogeneity of the Mn redox.[49,50] In addition, sXAS spectra of the Fe L-edges confirm the reversible redox process of Fe^{3+}/Fe^{4+}.

To investigate the possible participation of oxygen redox in the charge compensation mechanism, both the total fluorescence yield (TFY) mode and total electron yield (TEY) mode of sXAS for O K-edge were measured (Figure 3d,e). Figure 3f shows the comparison of the integrated area under the O K-edge pre-edge (528–533 eV) at different states during the first cycle in the TFY mode. The pre-edge peaks below 533 eV are attributed to transitions from the O 1*s* to the empty transition-metal *d* orbitals mixed with O 2*p* orbitals which are the states of most interest to us here, whereas the broad peaks correspond to O 2*p*-TM 4*sp* hybridized states. In TEY and TFY modes, a peak of 533.5 eV in the O-K edge spectrum is designated to Na_2CO_3. This peak disappears during charging and reappears when the cell is discharged to 1.5 V. In Figure 3f, it can be seen that the pre-edge peak changes in the area

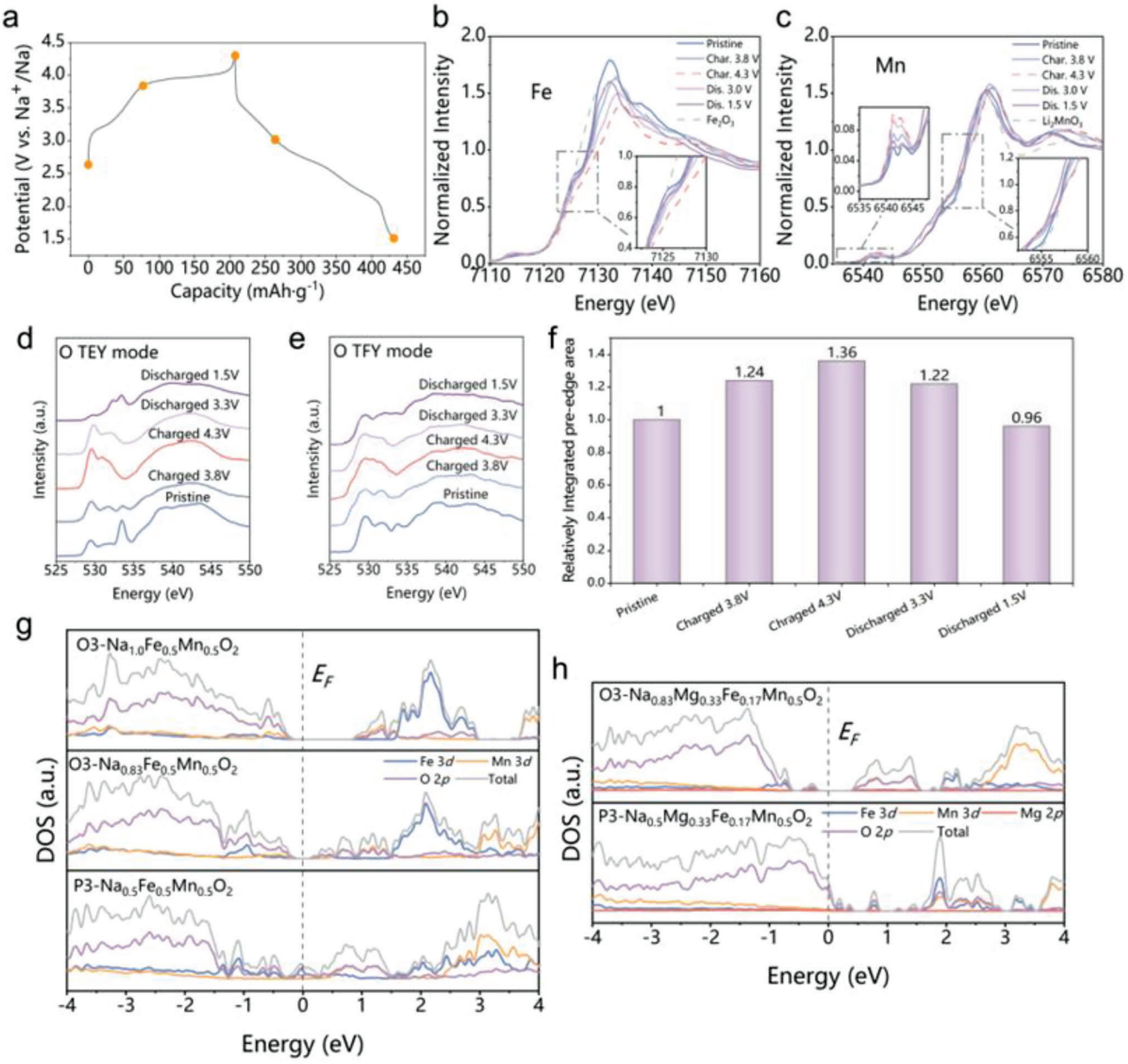

Figure 3. Charge compensation mechanism of NaMFM during cycling. a) Charge–discharge curves and corresponding points of NaMFM electrode for taking ex situ XAS measurement. b) Fe and c) Mn K-edge XANES of NaMFM at various states in the first cycle. d) TEY mode and e) TFY mode of oxygen K-edge soft XAS spectra at different states of NaMFM. f) Comparison of the integrated area under the pre-edge (from 528 to 533 eV) of the O K-edge XAS during the first cycle derived from TFY mode. g,h) Projected density of states (PDOS) for pristine samples of $NaFe_{0.5}Mn_{0.5}O_2$ and $Na_{0.83}Mg_{0.33}Fe_{0.17}Mn_{0.5}O_2$, as well as charged samples of $Na_{0.83}Fe_{0.5}Mn_{0.5}O_2$, $Na_{0.5}Fe_{0.5}Mn_{0.5}O_2$, and $Na_{0.5}Mg_{0.33}Fe_{0.17}Mn_{0.5}O_2$.

under the spectra during charge, suggesting that O 2*p* holes and the average effective charge increase remarkably, implying that oxygen contributes to the charge compensation during charging. During discharge, the integrated area of the pre-edge peak decreases, indicating the high reversibility of oxygen redox in MFM. As evidenced by the O K-edge sXAS spectra, the reversible oxygen redox is present in MFM throughout the entire voltage range during both charge and discharge.[24]

The evolution of the Fourier-transformed extended X-ray absorption fine structure (FT-EXAFS) spectra in different charge-discharge states are shown in Figure S12a,b (Supporting Information). Two intense peaks in the Fe and Mn K-edges are observed, which correspond to the average TM-O length of the first shell TM-O_6 configuration and the TM-TM length of the second shell TM-TM_6 on the *ab*-plane, respectively. Figure S12a (Supporting Information) shows that the Fe–O bond length undergoes a reversible decrease/increase upon desodiation/sodiation, indicating the Fe^{3+}/Fe^{4+} oxidation/reduction. For Mn–O bond (Figure S12b, Supporting Information), subtle variations were only observed up to 4.3 V, and the Mn–O interatomic distance of

the fully sodiated sample shows a slight change compared with that of the pristine sample, which reveals that the valence of Mn remains +4 during the charging process and Mn^{4+} is reduced to Mn^{3+} during the discharging process. For the second coordination shells, all of the TM–TM interatomic distances decrease with the oxidation of TM-ions and increase with the reduction of TM-ions, indicating a random and uniform distribution of TM-ions. It should be noted that the distinct shift of TM–O peaks is also an indicator of the change in oxygen ions, which reveals the contribution of oxygen in charge compensation.

To gain further insight into the role of Mg-doping in the redox mechanism, we conducted density functional theory (DFT) calculations to obtain the projected density of states (PDOS) for pristine samples of $NaFe_{0.5}Mn_{0.5}O_2$ and $Na_{0.83}Mg_{0.33}Fe_{0.17}Mn_{0.5}O_2$, as well as charged samples of $Na_{0.83}Fe_{0.5}Mn_{0.5}O_2$, $Na_{0.5}Fe_{0.5}Mn_{0.5}O_2$, and $Na_{0.5}Mg_{0.33}Fe_{0.17}Mn_{0.5}O_2$. As shown in Figure 3g,h, the PDOS structures of $NaFe_{0.5}Mn_{0.5}O_2$, $Na_{0.83}Fe_{0.5}Mn_{0.5}O_2$ and $Na_{0.83}Mg_{0.33}Fe_{0.17}Mn_{0.5}O_2$ exhibit bandgap values of ≈1.0, 0.2, and 0.5 eV, respectively, whereas the PDOS structures of $Na_{0.5}Fe_{0.5}Mn_{0.5}O_2$ and $Na_{0.5}Mg_{0.33}Fe_{0.17}Mn_{0.5}O_2$ exhibit metallic behavior. The electronic states near the Fermi level in $Na_{0.5}Fe_{0.5}Mn_{0.5}O_2$ are mostly Fe *d* orbital character, while those in $Na_{0.5}Mg_{0.33}Fe_{0.17}Mn_{0.5}O_2$ are mainly dominated by O *p* orbitals near the Fermi level. The electronic density of states contributed by O *p* orbitals near the Fermi level in $Na_{0.5}Mg_{0.33}Fe_{0.17}Mn_{0.5}O_2$ is much larger than that in $Na_{0.5}Fe_{0.5}Mn_{0.5}O_2$, indicating higher anionic redox activity of O^{2-}/O^{-} and the contribution to the additional specific capacity during charging process in the former Mg-doped compound. Moreover, by comparing the PDOS of $Na_{0.5}Fe_{0.5}Mn_{0.5}O_2$ and $Na_{0.5}Mg_{0.33}Fe_{0.17}Mn_{0.5}O_2$, we observe that Mg plays a dominant role in enhancing the electronic density of states of O *p* orbitals near the Fermi level and thereby activating the anionic redox activity of O^{2-}/O^{-}.

2.4. Crystal Structure Evolution

To elucidate the reaction mechanism and changes in the crystal structure of NaMFM caused by Na^+ intercalation/deintercalation, *operando* XRD was performed during the first two cycles, with the findings shown in **Figure 4**a. Due to the relatively low Na content of NaMFM, the phase transition occurs immediately after the charging process begins. The (003) and (006) peaks associated with the pristine O3 phase shift to a lower angle and split into two, followed by the appearance of a set of new peaks associated with a hexagonal P3 phase at a lower angle. The shift and appearance of the new peaks indicate that the *c* axis expands due to the increased repulsion force between adjacent oxygen layers when Na^+ is extracted, and in the same region, the $(104)_{O3}$ peak shifts to a higher angle since the in-plane TM–TM bond length decreases, suggesting the oxidation of transition metals. When the cell was continuously charged to 3.4 V, the O3 peaks vanished completely and all diffraction lines were assigned to the P3 phase, which proceeded until the cell was charged to 4.0 V, showing a single-phase reaction in this region, consistent with the slope change curve. As Na^+ was extracted further, a new phase "X" was observed, and the X phase presented broad peaks whose intensity decreased as Na was removed.[51] When further charged to the end, the peak at ≈17° shifts continuously to higher angles upon deintercalation, indicating a contraction of the interslab distance. The contraction may correlate with cation migration and the oxidation of O, resulting in decreased repulsion, as previously reported for $LiCoO_2$ or Ni-rich Li-based layered oxides.[11] As illustrated in Figure 4a, several distinct asymmetric diffraction patterns were observed, particularly in the X region. This asymmetric broadening was induced by the systematic sliding of the TM layers, which could have resulted in stacking faults. Upon discharging, the XRD pattern experiences a direct evolution from "X" to O3 without transforming to P3, and the broader diffraction peaks compared to the peaks of the pristine O3 phase imply a decrease in crystallinity after one full cycle, which might be related to Fe-migration. The irreversible phase transition during the first cycle may be responsible for the capacity loss between the first two cycles. On the second charge, the O3 phase changes directly to the "X" phase without the presence of the P3 phase, which is completely different from the first charge process, and the "X" phase transforms back to O3 phase upon discharge, restoring the well-defined peaks corresponding to the O3 phase to their initial discharge positions. The discrepancy in the phase transition behavior observed between the first and second charge processes is likely responsible for the disappearance of the plateau region (Figure 2a and Figure S5a, Supporting Information).

We conducted HAADF-STEM imaging to visualize the "X" phase at the atomic resolution. Figure 4b–e illustrates the stacking of the TMO_2 slabs along the [100] projection for the pristine NaMFM and three ex situ samples (charged to 3.8 V, 4.3 V and discharged to 1.5 V). The atomic columns seen in the image are a result of the transition metals in the structure since the contrast of the HAADF mode is sensitive to the atomic number of periodic atoms. In the pristine material (Figure 4b), the bright spots representing TM columns are well stacked, indicating the fine-layered structure of the raw materials. The interlayer distance between transition metals in distinct layers is ≈5.4 Å. Figure 4c shows HAADF-STEM image of the sample charged to 3.8 V. The structure can be assigned to the P3 phase due to the weak Na contrast, which occurs due to the disordering of Na over two prismatic sites available in the P3 structure.[19] The distance between adjacent TM layers is ≈5.6 Å. In contrast, the image of the sample charged to 4.3 V (Figure 4d) shows aligned adjacent layers (green line) and offset adjacent layers (yellow line), which can be indexed with the O1 and P3 phases, respectively.[51] This implies that the X phase is composed of the domains of the P3 and O1 structures. A nanoscale intergrowth is generated by the domains that are only a few units wide or possibly only one layer wide. Cation migration into the interlayer is observed in O1 domains (marked with red circles), which can well explain the continuous shift of the (00l) peak to higher angles observed in *operando* XRD as cation migration induces interlayer contraction. The HAADF-STEM intensity profiles across the layers can also be used to determine the presence or absence of the transition-metal cations in the interlayer cavities of the O1 and P3 domains, respectively. The P3 domain has a larger interlayer spacing of ≈5.0 Å compared to ≈4.7 Å in the O1 domains. When discharged to 1.5 V (Figure 4e), the well-ordered O3 stacking sequence is restored, with an interlayer spacing of ≈5.3 Å. A smaller interlayer distance compared to pristine samples is caused by the reduction of Mn^{4+} during discharge.

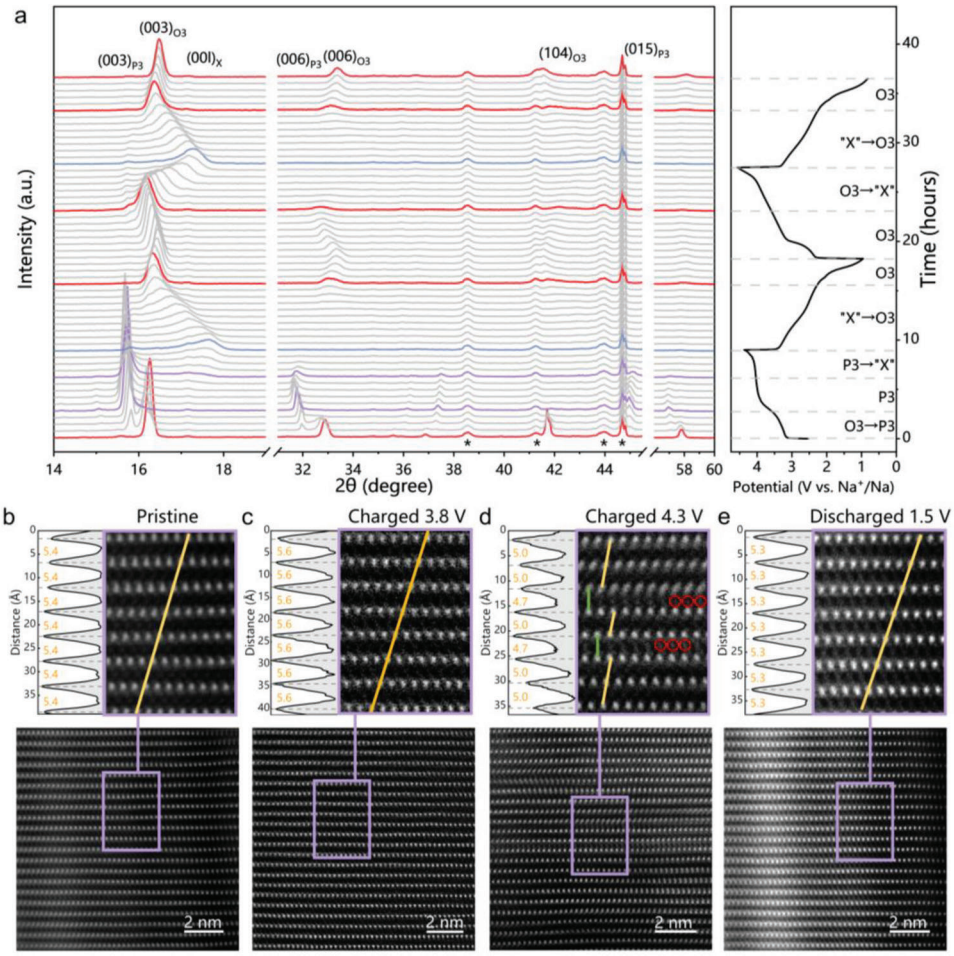

Figure 4. Structural evolution. a) *Operando* XRD patterns collected during the first two charge/discharge process of the O3-NaMFM electrode cycled between 1.5 and 4.3 V at a current of 20 mA g^{-1}. Atomic resolved HAADF-STEM images obtained from pristine NaMFM and three different states of charge: b) pristine, c) charged to 3.8 V, d) charged to 4.3 V, and e) discharged to 1.5 V. All of the images are taken along the [100] projection. The highlighted region of each image clearly shows the stacking of the layers which are identified as either P-type (no TM offset: green line) or O-type (TM offset: orange line). The intensity variation is plotted to the left of each highlighted image in order to measure the interlayer distances between adjacent TMO_2 slabs.

MS was used to obtain a clearer view of the involvement of Fe in phase transition and charge compensation. For the NaMFM compositions, the spectra of the pristine materials (**Figure 5**a), fully charged materials (Figure 5b), and fully discharged materials (Figure 5c) were obtained at room temperature in sealed sample holders. The isomer shift (IS), quadrupole splitting (QS), and relative concentrations of Fe^{3+}/Fe^{4+} ions are presented in **Table 1**. All spectra show an apparent quadrupole doublet whose asymmetry, shift, and splitting vary with the state of charge.

As expected, the spectrum of the pristine sample (Figure 5a) was composed of a single sharp doublet with IS and QS. The IS and QS values are 0.3628 and 0.6665 mm s^{-1}, respectively, consistent with high-spin Fe^{3+} ($S = 5/2$) in FeO_6 octahedral environment. In Figure 5b, the asymmetric spectrum of the charged materials shows that the removal of Na ions (charging) results in the formation of an asymmetry in the doublet, with additional spectral weight shifted to negative velocity. The spectrum was fitted using three components (Table 1). The main component with major intensity is attributed to $Fe^{3+}O_6$ in an octahedral environment and has a smaller isomer shift value of 0.3019 mm s^{-1} and larger quadrupole splitting values of 0.8260 mm s^{-1} compared to its pristine counterpart. The change in the IS parameter to more negative values upon charging is consistent with an increase in electron density at the Fe nuclei as the Fe–O bonds contract, which agrees with observed contraction in the in-plane TM–TM distance (*a*-parameter) in the *operando* XRD and ex situ EXAFS. In addition, the larger quadrupole splitting (QS) for the Fe^{3+} signal is attributed to the increased distortion of the octahedral environment within the TM layers. The second component with an isomer shift close to zero and a quadrupole splitting of 0.4287 mm s^{-1} is consistent with $Fe^{4+}O_6$ in sodium layered oxides. This is consistent with the changes in the XANES Fe K-edge and soft XAS Fe $L_{2,3}$-edge discussed previously. It should be mentioned that the amount of tetravalent iron ions is smaller than the expected value deduced from the electrochemical deintercalation. Given the fact that this material was collected at 4.3 V versus Na/Na^+, the measured value could be less than the true value due to electrolyte decomposition.[30] The third component with

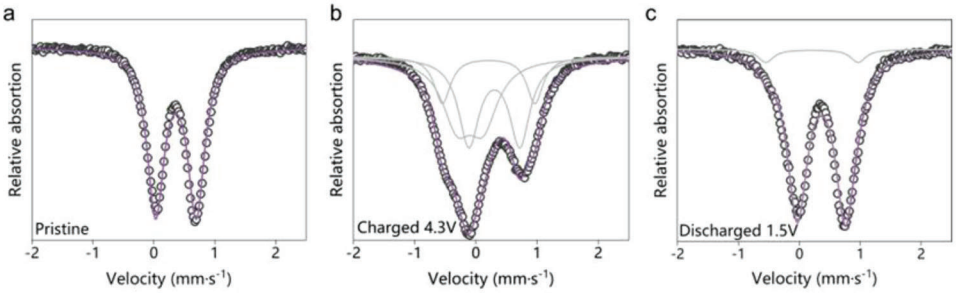

Figure 5. ^{57}Fe-Mössbauer spectroscopy spectra at various states of charge. a) Pristine, b) charged to 4.3 V, and c) discharged to 1.5 V. Raw data are shown in black. Individual spectral components of $Fe^{3+}O_6$, $Fe^{3+}O_4$, and $Fe^{4+}O_6$ from fitting are shown in gray, and the purple line represents the total fit.

Table 1. ^{57}Fe-Mössbauer spectroscopy parameters.

	Component	IS [mm s^{-1}]	QS [mm s^{-1}]	Area [%]
Pristine	$Fe^{3+}O_6$	0.3628	0.6665	100
Charged4.3 V	$Fe^{3+}O_6$	0.3019	0.8260	42.19
	$Fe^{4+}O_6$	-0.0943	0.4287	38.92
	$Fe^{3+}O_4$	0.2081	1.5110	18.89
Discharged 1.5 V	$Fe^{3+}O_6$	0.3608	0.7900	94.24
	$Fe^{3+}O_4$	0.2072	1.5135	5.76

an isomer shift of 0.2081 mm s^{-1} and a large quadrupole splitting of 1.511 mm s^{-1} is assigned to $Fe^{3+}O_4$ (tetrahedral coordination) owing to the non-centrosymmetry of its ligand environment. It should be mentioned that the intensity we derived here (18.89%) may be slightly overestimated because the peak broadening could also be caused by the decrease in crystallinity as a consequence of the phase transition from the O3 to the "X" phase, which is supported by the general peak broadening observed in the *operando* XRD. In Figure 5c, the spectrum of the discharged material was fitted using two components. The major intensity is attributed to $Fe^{3+}O_6$, while the second component is consistent with $Fe^{3+}O_4$. The fitting result indicates that the Fe-migration that occurs during the first charge process is mostly reversible. In conjunction with the cation migration observed in the HAADF-STEM images, this could explain the irreversible phase change shown in in situ XRD that the residual Fe remaining in the Na layer anchored the interlayer glide and blocked the Na diffusion pathway, which led to the capacity loss and voltage hysteresis observed in the first two cycles.

3. Conclusion

In conclusion, phase-pure $Na_{0.83}Mg_{0.33}Fe_{0.17}Mn_{0.50}O_2$, with a minor sodium deficiency compared to O3-$NaFe_{0.5}Mn_{0.5}O_2$, was synthesized and used as a cathode material in Na-ion half-cells and full-cells. A high charge capacity of ≈210 mAh g^{-1} and discharge capacity of ≈220 mAh g^{-1} in half cells was achieved in 1.5–4.3 V at 10 mA g^{-1}. *Operando* XRD reveals unique phase transformations that differ from other typical Na-ion layered oxide cathodes, which are found to be different for the first and second charge cycles. Mössbauer spectroscopy further confirms that Fe migration into the Na layer tetrahedral site during the first charge process is mostly reversible. The STEM image shows a direct view of the high voltage phase "X" with cation migration, which explains the "X" phase is composed of the domains of the P3 and O1 structures, just as previously reported.[51] During the Na-deintercalation at high voltage region, the randomly distributed Na-deficiency layer transforms from P to O type, which gives the pathway for Fe migration. The migrated Fe induces interlayer contraction, and residual migrated Fe makes it more difficult to restore the crystallinity, culminating in capacity loss and material failure. Ex-situ hXAS and sXAS explain Fe, Mn, and O redox participation by both K/L-edge and pre-edge peak centroid shifts. Operando DEMS confirms that the Mg substitute strategy is a more effective way to activate oxygen redox reaction without oxygen release.

This study reports a potential Ni- and Co-free, Fe and Mn-based Na-ion cathode material with no requirement for additional sacrificial salt or electrochemical pre-sodiation for full-cell operation. The Fe and Mn-based cathodes are particularly attractive because of the abundance of Fe/Mn on Earth, and such cathodes are complementary resource-wise to the LIB technology, which is highly dependent on Li, Ni, and Co. The incompletely reversible migration of Fe, which is the primary cause of large cell polarization and structural failure in such material, must be addressed in order to improve its performance for future applications. Namely, it can be suppressed by increasing the activation energy of Fe migration through doping elements or by suppressing the P-O phase transition occurring at high voltage. These findings provide new opportunities to design cathode materials toward reversible oxygen redox with high structural stability.

4. Experimental Section

Material Synthesis: $Na_{0.83}Mg_{0.33}Fe_{0.17}Mn_{0.50}O_2$ and $NaFe_{0.5}Mn_{0.5}O_2$ were synthesized by a solid-state reaction. For the $Na_{0.83}Mg_{0.33}Fe_{0.17}Mn_{0.50}O_2$, stoichiometric precursors of Na_2CO_3 (Alfa, 99.5%), MgO (Aladdin, >97%), MnO_2 (Aladdin, 98%), and Fe_2O_3 (Aladdin, 99.9%) were thoroughly mixed in an agate mortar and pressed into pellets under a pressure of 10 MPa, which were then calcined at 900 °C for 15 h in air and naturally cooled to room temperature. For the $NaFe_{0.5}Mn_{0.5}O_2$, stoichiometric precursors of Na_2CO_3 (Alfa, 99.5%), Mn_2O_3 (Aladdin, 98%), and Fe_2O_3 (Aladdin, 99.9%) were properly mixed in an agate mortar and pressed into pellets under a pressure of 10 MPa,

which were then calcined at 850 °C for 15 h in air and quenched to room temperature in a copper jar. Following the heat treatment, both materials were transferred to an Ar-filled glovebox to avoid exposure to moisture. It should be noted that no excess Na_2CO_3 was used in the synthesis.

Electrochemical Measurements: The cathode films used in the half-cell tests were prepared by mixing the active material, carbon nanotubes, and polytetrafluoroethylene (PTFE) at a weight ratio of 8:1:1 inside a glovebox. After mixing, the components were rolled into thin films with a loading mass of 8–10 mg cm^{-2}. For the cathode used in the full cell test, a slurry was prepared by mixing the active material, acetylene black, and polyvinylidene fluoride (PVDF) in a weight ratio of 70:20:10. The slurry was then spread on an aluminum (Al) foil with a loading mass of ≈10 mg cm^{-2}. HC anodes were prepared by spreading a slurry consisting of hard carbon (HC), sodium alginate binder, and acetylene black (92:4:4) on Al foil for full-cells, with ≈2.5 mg cm^{-2} of active anodes. After drying at 100 °C under vacuum for 12 h, the electrodes were fabricated into CR2032 coin-type cells in an argon-filled glove box (H_2O, O_2 < 0.1 ppm). Glass fibers and sodium metal/HC were used as separators and counter/reference electrodes, respectively. 1 M $NaClO_4$ in PC with FEC (2% in volume) was used as the electrolyte. Charge and discharge measurements were conducted on the Land CT2001A battery test system (Wuhan, China) at various voltage windows. The full cells were charged and discharged in the voltage range of 1.0–4.3 V with a N/P ratio of 1.1. The galvanostatic intermittent titration technique (GITT) was measured by applying the repeated current pulses for 30 min at a current density of 10 mA g^{-1} followed by relaxation for 3 h. The cyclic voltammetry and the linear sweep voltammetry data were recorded on a CH Instruments Electrochemical Workstation at a scan rate of 0.1 mV s^{-1}.

Material Characterization: Powder XRD was performed using a Bruker D8 Advance diffractometer equipped with a Cu Kα radiation source (λ_1 = 1.54060 and λ_2 = 1.54439 Å) and a LynxEye_XE detector. The NPD experiments and the nPDF experiments were carried out on Multi-Physics Instrument (MPI), a total scattering neutron time-of-flight diffractometer at CSNS, Dongguan, China. Each sample was put into a ZrTi alloy tank with a diameter of 8.9 mm and the diffraction patterns were collected within the neutron wavelength range from 0.1 to 4.5 Å. Then the GSAS-II program was used to analyze the crystal structure by the Rietveld refinement methods. The pseudo-Voigt peak function was chosen to fit the entire pattern. The high quality of diffraction data ensures reliable results for crystal structures.[52] The nPDF patterns were obtained by the Fourier transform of the reduced structure function which is merged in the Q range from 1.05 to 25 $Å^{-1}$. The data were collected at room temperature under vacuum and then analyzed by full pattern refinement method. Data are fitted using the open-source software PDF-gui.[53] The morphology of the material was characterized on a scanning electron microscope (Hitachi S-4800) equipped with an EDX detector for element analysis. The actual chemical composition of the final materials was analyzed by inductively coupled plasma-atomic emission spectroscopy (ICP-AES, Shimadzu, ICPS-8100). Aberration-corrected STEM observation was carried out on a JEOL ARM200CF transmission electron microscope equipped with double aberration correctors. Atomic resolved HAADF and ABF STEM images were captured with a convergent angle of 28 mrad and acceptance angle of 90–370 and 11–23 mrad, respectively. Hard XAS was conducted on beamline BL14W1 in the Shanghai Synchrotron Radiation Facility (SSRF). Data from XANES and EXAFS were processed using the software package Athena.[54] The sXAS measurements through both TEY and TFY modes of Fe, Mn $L_{2,3}$, and O K edges were recorded at beamline 02B at SSRF. The sodiated/desodiated samples were prepared electrochemically. Transmission MS at room temperature were recorded using a conventional spectrometer working in constant acceleration mode with a γ-ray source of 25 mCi ^{57}Co/Rh vibrating at room temperature. The drive velocity was calibrated using sodium nitroprusside (SNP) powder and the isomer shifts (IS) quoted in this work are relative to that of the α-Fe foil at room temperature. All the MS data were analyzed with the MossWinn 4.0 program.[55] All the samples were transferred under proper protection in any of the above tests.

The *operando* XRD signals were collected on an X'Pert Pro MPD X-ray diffractometer (D8 Advance with a LynxEye_XEdetector, Bruker) with Cu Kα1 radiation (λ = 1.5405 Å) and metal aluminum (Al) metal as the window of a specially designed electrochemical cell. PTFE was used as the binder of the current-collector-free electrode. The cell was cycled between 1.5 and 4.3 V versus Na^+/Na at a current density of 10 mA g^{-1}.

The *operando* DEMS was performed in a special cell model and instrument. The mass loading of the active material for each electrode is about 7 mg cm^{-2}. The special cell model was assembled in a glovebox filled with argon gas, using Celgard 2400 membrane as the separator, and 1 M $NaClO_4$ in PC with FEC (2% in volume) as the electrolyte and sodium metal as the anode. The charging process was tested on the Land CT2001A battery test system (Wuhan, China) at 0.05 C. The Agilent 7890B/5977A series Gas Chromatograph/Mass Selective (GCMS) Detector (carrier gas: argon, 2.25 µL min^{-1} at 0.2 MPa) was utilized for gas acquisition.

First-Principles Calculations: In this work, DFT calculations were performed using Vienna Ab-initio Simulations Package (VASP) code[56,57] with the Perdew–Burke–Ernzerhof (PBE)[58] generalized gradient approximation (GGA).[59] To take into account the strong electronic correlation effects of transition-metal *3d* electrons, the GGA+*U* method was adopted and the effective *U* value of Fe and Mn was set to 4.6 and 5.0 eV.[60] The DFT calculations used 4 × 3 × 2 k-point grid and energy cutoff of 500 eV. All ions were fully relaxed in the optimization with the energy and force convergence criterion of 10^{-5} eV and 0.03 eV $Å^{-1}$, respectively. For $NaFe_{0.5}Mn_{0.5}O_2$, $Na_{0.83}Fe_{0.5}Mn_{0.5}O_2$, and $Na_{0.83}Mg_{0.33}Fe_{0.17}Mn_{0.5}O_2$, the calculations were based on the supercell obtained by 2 × 3 × 1 expansion of the conventional cell O3-$NaFeO_2$ (R-3m), including 18 Na, 9 Fe, 9 Mn, 36 O atoms, and 15 Na, 9 Fe, 9 Mn, 36 O atoms, and 15 Na, 6 Mg, 3 Fe, 9 Mn, 36 O atoms, respectively. For $Na_{0.5}Fe_{0.5}Mn_{0.5}O_2$ and $Na_{0.5}Mg_{0.33}Fe_{0.17}Mn_{0.5}O_2$, the calculations were based on the supercell obtained by 2 × 3 × 1 expansion of the conventional cell P3-Na_xFeO_2 (R3m), including 9 Na, 9 Fe, 9 Mn, 36 O atoms, and 9 Na, 6 Mg, 3 Fe, 9 Mn, 36 O atoms, respectively.

Supporting Information

Supporting Information is available from the Wiley Online Library or from the author.

Acknowledgements

This work was supported by the National Key R&D Program of China, National Natural Science Foundation (NSFC) of China (51725206, 52122214, and 52002394), Youth Innovation Promotion Association of the Chinese Academy of Sciences (2020006), and Beijing Municipal Natural Science Foundation (2212022). J.L. acknowledges support from Honda Research Institute USA, Inc.

Conflict of Interest

The authors declare no conflict of interest.

Author Contributions

Y-S.H. and X.R. conceived the project. J.L. developed the theory. Y.N. and Z.H. synthesized the materials and conducted the electrochemical measurements. X.D. conducted the STEM measurements. Y.N. and J.X. conducted NPD and nPDF measurements. Y.N. and L.Z. assembled and tested full cells. Y.N. and Y.L. conducted operando DEMS measurements. H.M. conducted DFT calculations. B.Z. and Z.L. conducted Fe-MS measurements. Y.N. and F.D. conducted XAS measurements. Y.N. analyzed the data. Y.N., X.R., J.L., and Y-S.H. wrote the paper. All authors discussed and contributed to the writing.

Data Availability Statement

The data that support the findings of this study are available from the corresponding author upon reasonable request.

Keywords

Fe/Mn-based layered oxides, Fe-migration, Mg substitution, Na-ion batteries, oxygen redox

Received: March 9, 2023
Revised: April 19, 2023
Published online: May 25, 2023

[1] H. Pan, Y.-S. Hu, L. Chen, *Energy Environ. Sci.* **2013**, *6*, 2338.
[2] *Nat. Energy* **2022**, *7*, 461.
[3] E. Gonzalo, M. H. Han, J. M. López del Amo, B. Acebedo, M. Casas-Cabanas, T. Rojo, *J. Mater. Chem. A* **2014**, *2*, 18523.
[4] B. Mortemard de Boisse, D. Carlier, M. Guignard, C. Delmas, *J. Electrochem. Soc.* **2013**, *160*, A569.
[5] N. Yabuuchi, M. Kajiyama, J. Iwatate, H. Nishikawa, S. Hitomi, R. Okuyama, R. Usui, Y. Yamada, S. Komaba, *Nat. Mater.* **2012**, *11*, 512.
[6] J.-J. Braconnier, C. Delmas, C. Fouassier, P. Hagenmuller, *Mater. Res. Bull.* **1980**, *15*, 1797.
[7] H. Yoshida, N. Yabuuchi, S. Komaba, *Electrochem. Commun.* **2013**, *34*, 60.
[8] J. Wang, B. Qiu, X. He, T. Risthaus, H. Liu, M. C. Stan, S. Schulze, Y. Xia, Z. Liu, M. Winter, J. Li, *Chem. Mater.* **2015**, *27*, 4374.
[9] D. Zhou, D. Ning, J. Wang, J. Liu, G. Zhang, Y. Xiao, J. Zheng, Y. Li, J. Li, X. Liu, *J. Energy Chem.* **2023**, *77*, 479.
[10] L. Mu, S. Xu, Y. Li, Y.-S. Hu, H. Li, L. Chen, X. Huang, *Adv. Mater.* **2015**, *27*, 6928.
[11] W. Xue, M. Huang, Y. Li, Y. G. Zhu, R. Gao, X. Xiao, W. Zhang, S. Li, G. Xu, Y. Yu, P. Li, J. Lopez, D. Yu, Y. Dong, W. Fan, Z. Shi, R. Xiong, C.-J. Sun, I. Hwang, W.-K. Lee, Y. Shao-Horn, J. A. Johnson, J. Li, *Nat. Energy* **2021**, *6*, 495.
[12] M. Yoon, Y. Dong, J. Hwang, J. Sung, H. Cha, K. Ahn, Y. Huang, S. J. Kang, J. Li, J. Cho, *Nat. Energy* **2021**, *6*, 362.
[13] C. Zhao, C. Li, H. Liu, Q. Qiu, F. Geng, M. Shen, W. Tong, J. Li, B. Hu, *J. Am. Chem. Soc.* **2021**, *143*, 18652.
[14] S. Guo, J. Yi, Y. Sun, H. Zhou, *Energy Environ. Sci.* **2016**, *9*, 2978.
[15] C. Zhao, Z. Yao, J. Wang, Y. Lu, X. Bai, A. Aspuru-Guzik, L. Chen, Y.-S. Hu, *Chem* **2019**, *5*, 2913.
[16] X. Rong, E. Hu, Y. Lu, F. Meng, C. Zhao, X. Wang, Q. Zhang, X. Yu, L. Gu, Y. S. Hu, H. Li, X. Huang, X. Q. Yang, C. Delmas, L. Chen, *Joule* **2019**, *3*, 503.
[17] *CRC Handbook of Chemistry and Physics* (Ed: W. M. Haynes), CRC Press, Boca Raton, FL **2016**.
[18] E. Boivin, R. A. House, M. A. Pérez-Osorio, J.-J. Marie, U. Maitra, G. J. Rees, P. G. Bruce, *Joule* **2021**, *5*, 1267.
[19] J. C. Kim, D. H. Kwon, J. H. Yang, H. Kim, S. H. Bo, L. Wu, H. Kim, D. H. Seo, T. Shi, J. Wang, Y. Zhu, G. Ceder, *Adv. Energy Mater.* **2020**, *10*, 2001151.
[20] J. Wang, D. Zhou, X. He, L. Zhang, X. Cao, D. Ning, B. Yan, X. Qi, J. Li, V. Murzin, E. Paillard, X. Liu, G. Schumacher, M. Winter, J. Li, *ACS Appl. Mater. Interfaces* **2020**, *12*, 5017.
[21] Q. Wang, S. Mariyappan, G. Rousse, A. V. Morozov, B. Porcheron, R. Dedryvère, J. Wu, W. Yang, L. Zhang, M. Chakir, M. Avdeev, M. Deschamps, Y.-S. Yu, J. Cabana, M.-L. Doublet, A. M. Abakumov, J.-M. Tarascon, *Nat. Mater.* **2021**, *20*, 353.
[22] D. Eum, B. Kim, S. J. Kim, H. Park, J. Wu, S.-P. Cho, G. Yoon, M. H. Lee, S.-K. Jung, W. Yang, W. M. Seong, K. Ku, O. Tamwattana, S. K. Park, I. Hwang, K. Kang, *Nat. Mater.* **2020**, *19*, 419.
[23] C. Zhao, Q. Wang, Z. Yao, J. Wang, B. Sánchez-Lengeling, F. Ding, X. Qi, Y. Lu, X. Bai, B. Li, H. Li, A. Aspuru-Guzik, X. Huang, C. Delmas, M. Wagemaker, L. Chen, Y.-S. Hu, *Science* **2020**, *370*, 708.
[24] X. Li, T. Wang, Y. Yuan, X. Yue, Q. Wang, J. Wang, J. Zhong, R. Lin, Y. Yao, X. Wu, X. Yu, Z. Fu, Y. Xia, X. Yang, T. Liu, K. Amine, Z. Shadike, Y. Zhou, J. Lu, *Adv. Mater.* **2021**, *33*, 2008194.
[25] Y. Yoda, K. Kubota, K. Kuroki, S. Suzuki, K. Yamanaka, T. Yaji, S. Amagasa, Y. Yamada, T. Ohta, S. Komaba, *Small* **2020**, *16*, 2006483.
[26] C. Ma, J. Alvarado, J. Xu, R. J. Clément, M. Kodur, W. Tong, C. P. Grey, Y. S. Meng, *J. Am. Chem. Soc.* **2017**, *139*, 4835.
[27] X. Yu, Y. Lyu, L. Gu, H. Wu, S. M. Bak, Y. Zhou, K. Amine, S. N. Ehrlich, H. Li, K. W. Nam, X. Q. Yang, *Adv. Energy Mater.* **2014**, *4*, 1300950.
[28] X. Rong, J. Liu, E. Hu, Y. Liu, Y. Wang, J. Wu, X. Yu, K. Page, Y. S. Hu, W. Yang, H. Li, X. Q. Yang, L. Chen, X. Huang, *Joule* **2018**, *2*, 125.
[29] J. W. Somerville, A. Sobkowiak, N. Tapia-Ruiz, J. Billaud, J. G. Lozano, R. A. House, L. C. Gallington, T. Ericsson, L. Häggström, M. R. Roberts, U. Maitra, P. G. Bruce, *Energy Environ. Sci.* **2019**, *12*, 2223.
[30] E. Lee, D. E. Brown, E. E. Alp, Y. Ren, J. Lu, J. J. Woo, C. S. Johnson, *Chem. Mater.* **2015**, *27*, 6755.
[31] E. Talaie, V. Duffort, H. L. Smith, B. Fultz, L. F. Nazar, *Energy Environ. Sci.* **2015**, *8*, 2512.
[32] Y. Li, Y. Gao, X. Wang, X. Shen, Q. Kong, R. Yu, G. Lu, Z. Wang, L. Chen, *Nano Energy* **2018**, *47*, 519.
[33] J. N. Zhang, Q. Li, Y. Wang, J. Zheng, X. Yu, H. Li, *Energy Storage Mater.* **2018**, *14*, 1.
[34] U. Maitra, R. A. House, J. W. Somerville, N. Tapia-Ruiz, J. G. Lozano, N. Guerrini, R. Hao, K. Luo, L. Jin, M. A. Pérez-Osorio, F. Massel, D. M. Pickup, S. Ramos, X. Lu, D. E. McNally, A. V. Chadwick, F. Giustino, T. Schmitt, L. C. Duda, M. R. Roberts, P. G. Bruce, *Nat. Chem.* **2018**, *10*, 288.
[35] R. A. House, U. Maitra, L. Jin, J. G. Lozano, J. W. Somerville, N. H. Rees, A. J. Naylor, L. C. Duda, F. Massel, A. V. Chadwick, S. Ramos, D. M. Pickup, D. E. McNally, X. Lu, T. Schmitt, M. R. Roberts, P. G. Bruce, *Chem. Mater.* **2019**, *31*, 3293.
[36] E. Boivin, R. A. House, J.-J. Marie, P. G. Bruce, *Adv. Energy Mater.* **2022**, *12*, 2200702.
[37] E. De La Llave, E. Talaie, E. Levi, P. K. Nayak, M. Dixit, P. T. Rao, P. Hartmann, F. Chesneau, D. T. Major, M. Greenstein, D. Aurbach, L. F. Nazar, *Chem. Mater.* **2016**, *28*, 9064.
[38] M. Fan, Y. Chen, Y. Xie, T. Yang, X. Shen, N. Xu, H. Yu, C. Yan, *Adv. Funct. Mater.* **2016**, *26*, 5019.
[39] S. Yuan, Y. H. Zhu, W. Li, S. Wang, D. Xu, L. Li, Y. Zhang, X. B. Zhang, *Adv. Mater.* **2017**, *29*, 1602469.
[40] N. Wang, Z. Bai, Y. Qian, J. Yang, *Adv. Mater.* **2016**, *28*, 4126.
[41] D. Y. W. Yu, P. V. Prikhodchenko, C. W. Mason, S. K. Batabyal, J. Gun, S. Sladkevich, A. G. Medvedev, O. Lev, *Nat. Commun.* **2013**, *4*, 2922.
[42] S. Peng, X. Han, L. Li, Z. Zhu, F. Cheng, M. Srinivansan, S. Adams, S. Ramakrishna, *Small* **2016**, *12*, 1359.
[43] Y. Fang, L. Xiao, J. Qian, Y. Cao, X. Ai, Y. Huang, H. Yang, *Adv. Energy Mater.* **2016**, *6*, 1502197.
[44] Y. N. Zhou, P. F. Wang, Y. Bin Niu, Q. Li, X. Yu, Y. X. Yin, S. Xu, Y. G. Guo, *Nano Energy* **2019**, *55*, 143.
[45] B. Zhang, R. Dugas, G. Rousse, P. Rozier, A. M. Abakumov, J. M. Tarascon, *Nat. Commun.* **2016**, *7*, 10308.
[46] Y. W. Tsai, B. J. Hwang, G. Ceder, H. S. Sheu, D. G. Liu, J. F. Lee, *Chem. Mater.* **2005**, *17*, 3191.
[47] F. Ding, Q. Meng, P. Yu, H. Wang, Y. Niu, Y. Li, Y. Yang, X. Rong, X. Liu, Y. Lu, L. Chen, Y. Hu, *Adv. Funct. Mater.* **2021**, *31*, 2101475.
[48] X. Liu, D. Wang, G. Liu, V. Srinivasan, Z. Liu, Z. Hussain, W. Yang, *Nat. Commun.* **2013**, *4*, 2568.
[49] L. Yang, Z. Liu, S. Liu, M. Han, Q. Zhang, L. Gu, Q. Li, Z. Hu, X. Wang, H.-J. Lin, C.-T. Chen, J.-M. Chen, S.-C. Haw, Z. Wang, L. Chen, *Nano Energy* **2020**, *78*, 105172.
[50] Y. Wang, J. Liu, B. Lee, R. Qiao, Z. Yang, S. Xu, X. Yu, L. Gu, Y. S. Hu, W. Yang, K. Kang, H. Li, X. Q. Yang, L. Chen, X. Huang, *Nat. Commun.* **2015**, *6*, 6401.

[51] S. Mariyappan, T. Marchandier, F. Rabuel, A. Iadecola, G. Rousse, A. V. Morozov, A. M. Abakumov, J. M. Tarascon, *Chem. Mater.* **2020**, *32*, 1657.
[52] B. H. Toby, R. B. Von Dreele, *J. Appl. Crystallogr.* **2013**, *46*, 544.
[53] C.-H. Liu, E. M. Janke, R. Li, P. Juhás, O. Gang, D. V. Talapin, S. J. L. Billinge, *J. Appl. Crystallogr.* **2020**, *53*, 699.
[54] B. Ravel, M. Newville, *J. Synchrotron Radiat.* **2005**, *12*, 537.
[55] Z. Klencsár, *AIP Conf. Proceedings* **2014**, *1622*, 30.
[56] G. Kresse, J. Furthmüller, *Phys. Rev. B* **1996**, *54*, 11169.
[57] G. Kresse, J. Furthmüller, *Comput. Mater. Sci.* **1996**, *6*, 15.
[58] J. P. Perdew, M. Ernzerhof, K. Burke, *J. Chem. Phys.* **1996**, *105*, 9982.
[59] J. P. Perdew, K. Burke, M. Ernzerhof, *Phys. Rev. Lett.* **1996**, *77*, 3865.
[60] F. Zhou, M. Cococcioni, C. A. Marianetti, D. Morgan, G. Ceder, *Phys. Rev. B* **2004**, *70*, 235121.

ADVANCED ENERGY MATERIALS

Supporting Information

for *Adv. Energy Mater.*, DOI 10.1002/aenm.202300746

Earth-Abundant Na-Mg-Fe-Mn-O Cathode with Reversible Hybrid Anionic and Cationic Redox

Yaoshen Niu, Zilin Hu, Bo Zhang, Dongdong Xiao, Huican Mao, Lin Zhou, Feixiang Ding, Yuan Liu, Yang Yang, Juping Xu, Wen Yin, Nian Zhang, Zhiwei Li, Xiqian Yu, Hao Hu, Yaxiang Lu, Xiaohui Rong*, Ju Li* and Yong-Sheng Hu**

Supporting Information

Earth-Abundant Na-Mg-Fe-Mn-O Cathode with Reversible Hybrid Anionic and Cationic Redox

Yaoshen Niu[1,2], Zilin Hu[2], Bo Zhang[3], Dongdong Xiao[2], Huican Mao[2], Lin Zhou[2], Feixiang Ding[2], Yuan Liu[2], Yang Yang[2], Juping Xu[4], Wen Yin[4], Nian Zhang[5], Zhiwei Li[3], Xiqian Yu[2], Hao Hu[1], Yaxiang Lu[2], Xiaohui Rong*[2], Ju Li*[6], Yong-Sheng Hu*[2]*

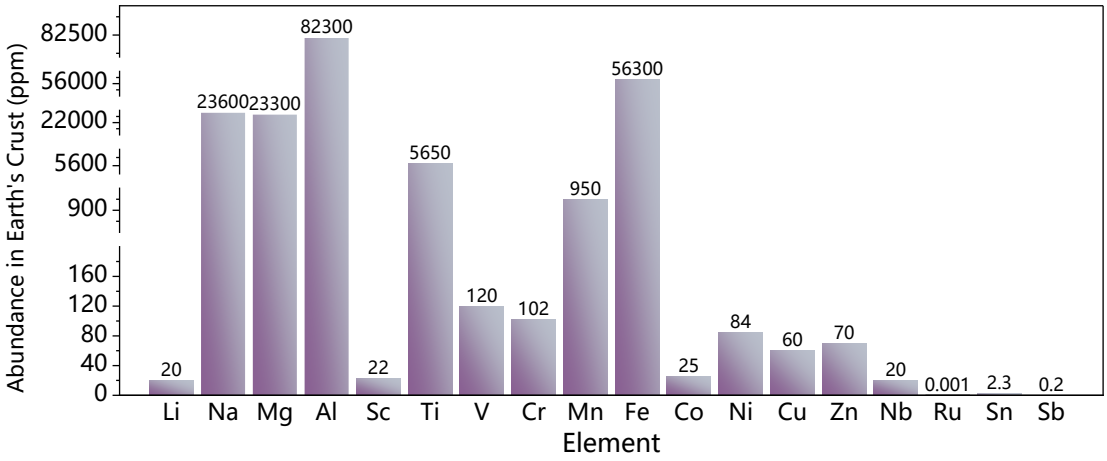

Figure S1. Comparison of elemental abundance in the Earth's crust for alkali and alkali-earth metal, transition metal, and p-block elements used as electrode materials for rechargeable NIBs.

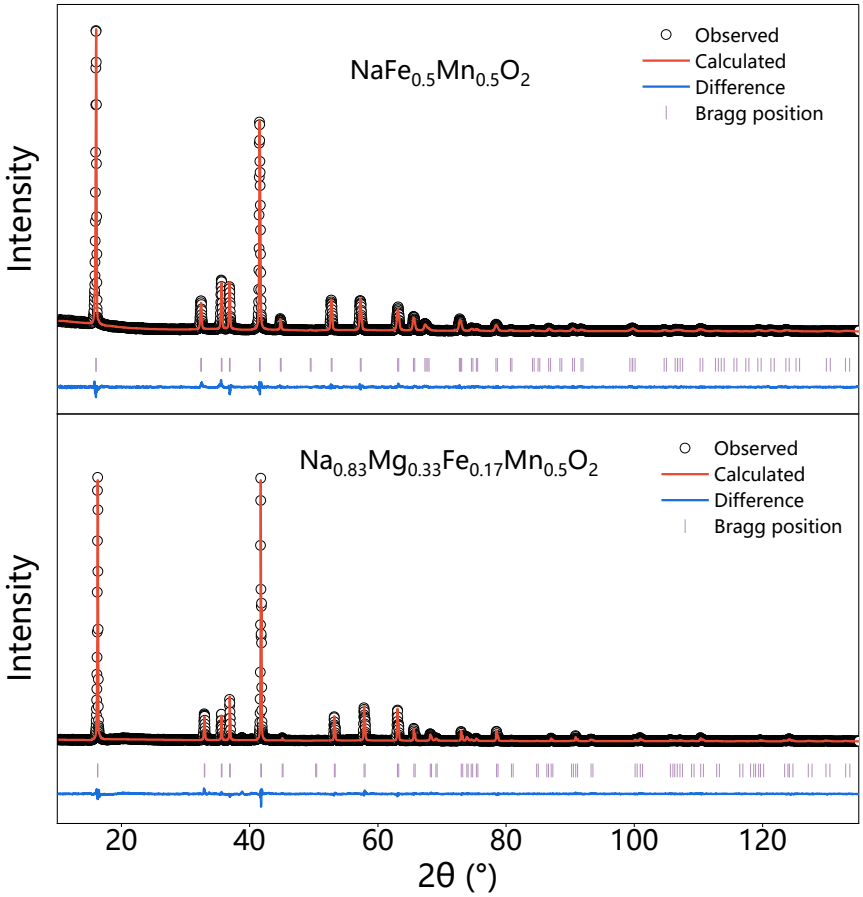

Figure S2 Refined XRD patterns of synthesized O3-NFM and O3-NaMFM samples. The observed changes in the (003)/(104) peak intensity ratio after Mg-doping can be attributed to both preferential orientation resulting from the sample preparation process for XRD analysis, as well as a reduction in the intensity of the (003) peak. The substitution of 1/3 of Fe with Mg (which has an atomic weight of 24.3 in contrast to Fe's atomic weight of 55.8) causes a decrease in the (003) peak intensity.

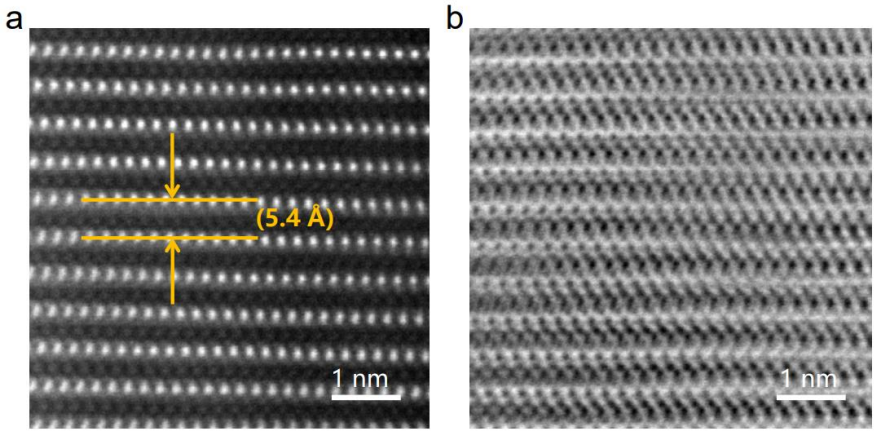

Figure S3 (a) Atomic-resolution high-angle annular dark field (HAADF) and (b) annular bright field (ABF) scanning transmission electron microscopy (STEM) images along the [100] zone axis.

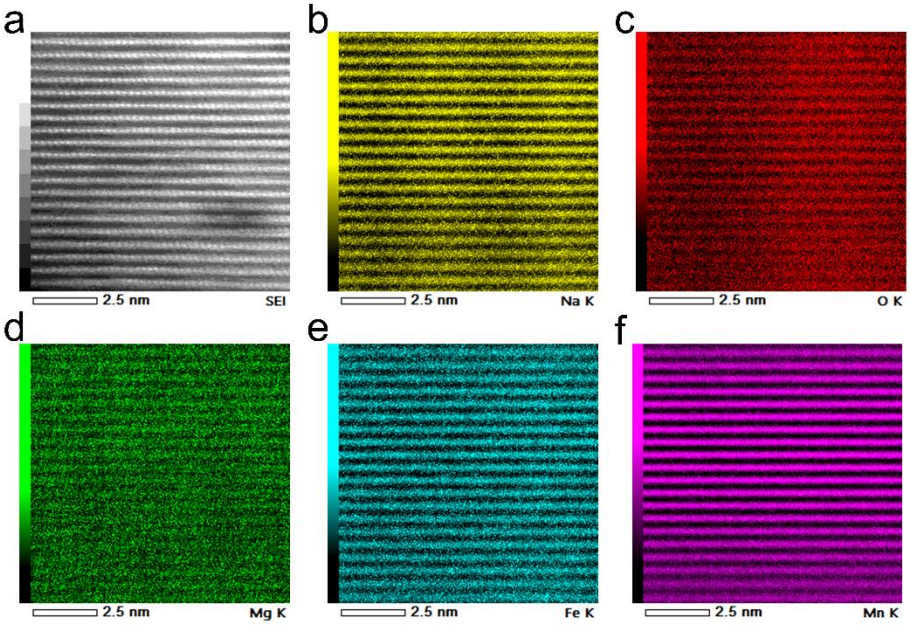

Figure S4 The atomic-scale EDS results of NaMFM samples along the [100] zone axis. Scale bar is 2.5 nm.

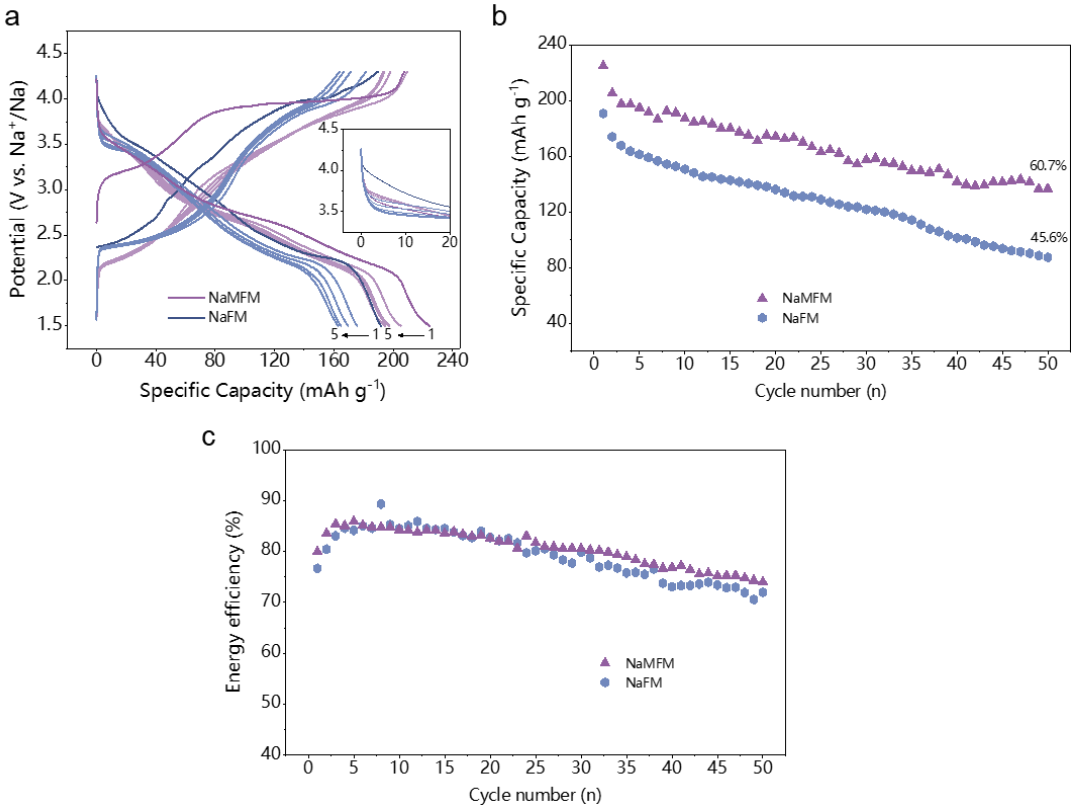

Figure S5 Comparison of (a) Galvanostatic charge and discharge profiles of the NaMFM/Na and NFM/Na half cells at 10 mA g-1 between 1.5-4.3 V along with associated (b) discharge capacities and (c) energy efficiency.

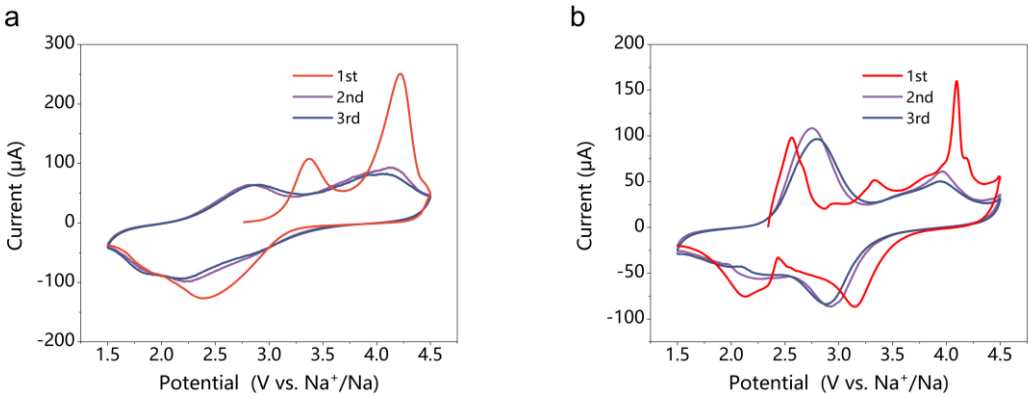

Figure S6 CV profiles of (a) NaMFM, (b) NaFM at a scan rate of 0.1 mV s^{-1} in the voltage range of 1.5-4.5 V.

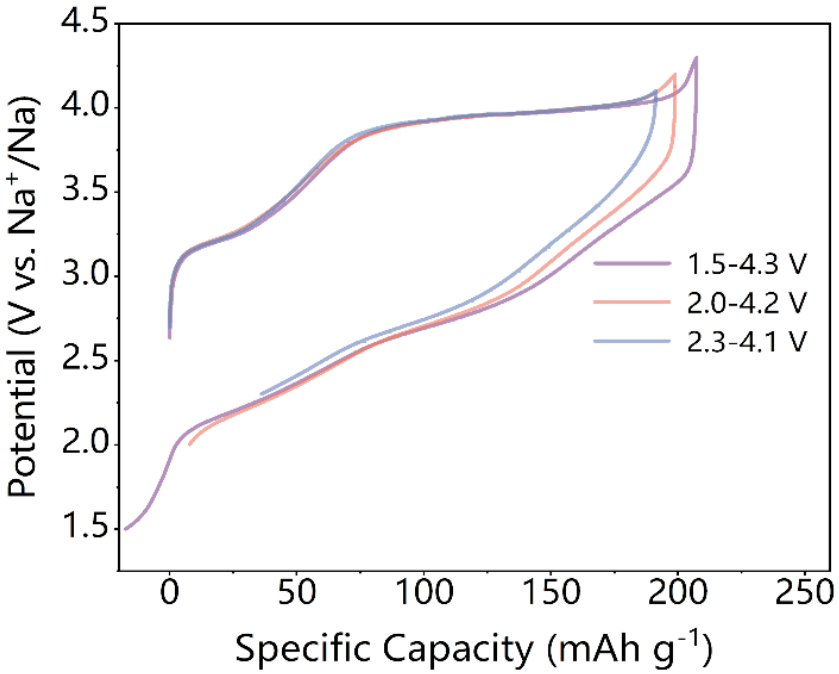

Figure S7 Comparison of galvanostatic cycling curves between different cycling window at 10 mA g^{-1}

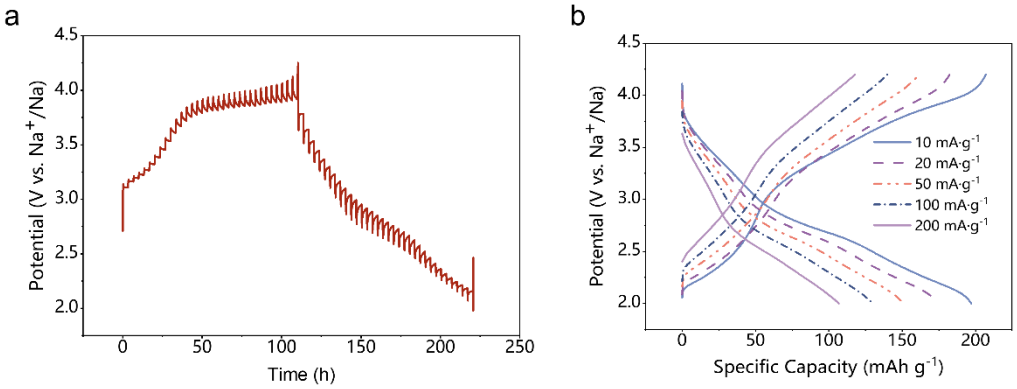

Figure S8 (a) GITT profiles for the first cycle of the O3-NaMFM sample. (b) Rate capability of NaMFM with current rates from 10 mA g^{-1} to 200 mA g^{-1} (2.0–4.2 V).

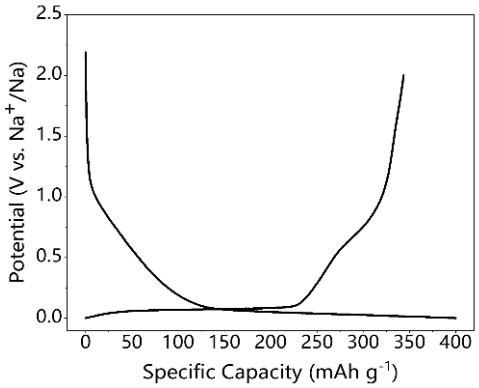

Figure S9 Galvanostatic charge and discharge profiles of the Hard carbon at 20 mA g^{-1} between 0-2 V for the first cycle.

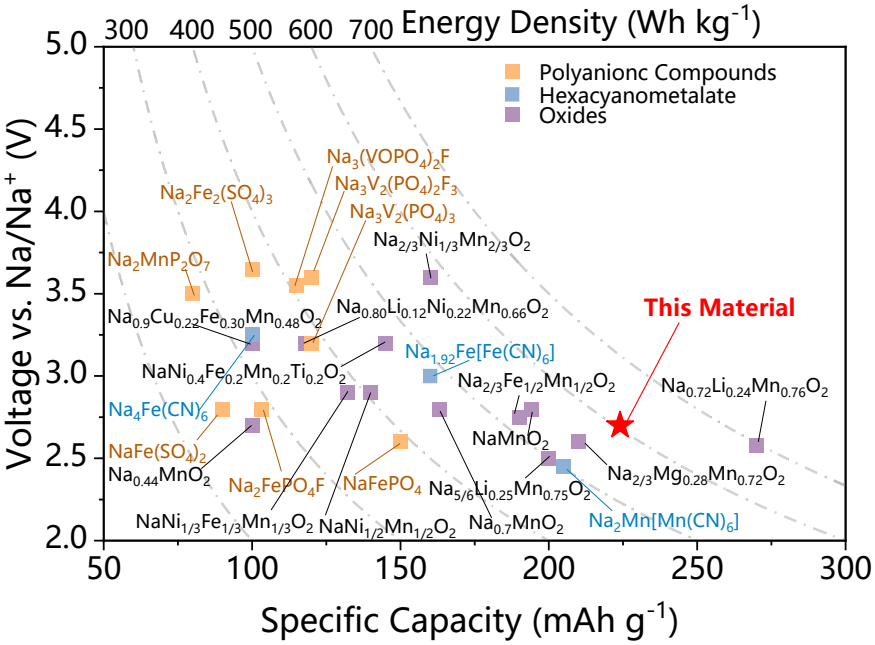

Figure S10 Comparisons of energy density between this work and other reported cathode materials for Na-ion batteries, which have been drawn based on the data in Table S4.

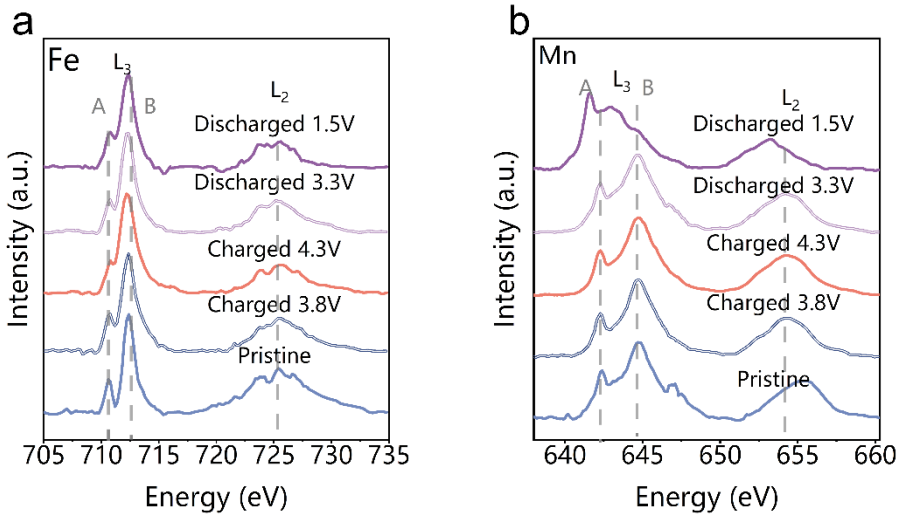

Figure S11 TEY mode of (a) Mn and (b) Fe $L_{2,3}$-edge soft XAS spectra at different states of NaMFM.

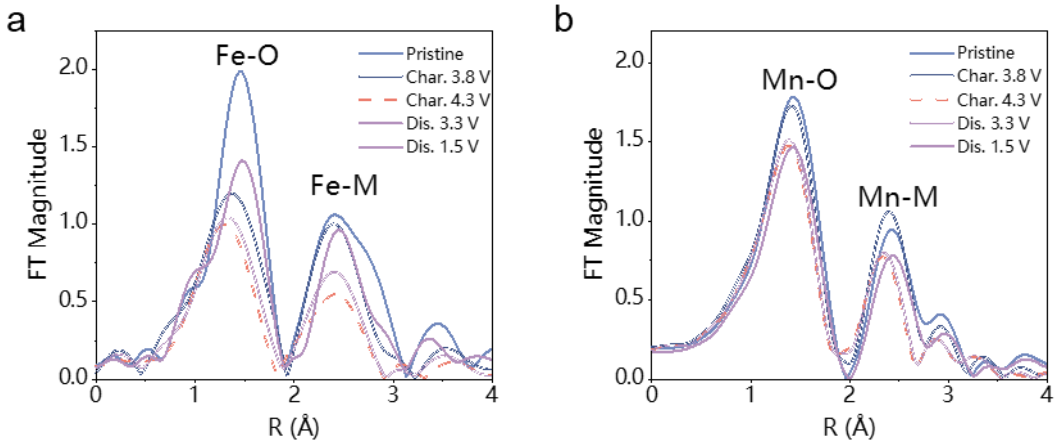

Figure S12 Ex situ EXAFS spectra at the (a) Fe K-edge and (b) Mn K-edge of NaMFM electrode collected at different charge/discharge states.

Table S1. Chemical composition of O3-$Na_{0.83}Mg_{0.33}Fe_{0.17}Mn_{0.50}O_2$ and O3-$Na_{1.0}Fe_{0.5}Mn_{0.5}O_2$ obtained by ICP-AES

Theoretical chemical formula	Measured atomic ratio			
	Na	Fe	Mn	Mg
$Na_{0.83}Mg_{0.33}Fe_{0.17}Mn_{0.50}O_2$	0.82(1)	0.17(1)	0.5	0.35(1)
$Na_{1.0}Fe_{0.5}Mn_{0.5}O_2$	0.98(1)	0.51(1)	0.5	0

Table S2. Crystallographic data and atomic positions of the O3-$Na_{1.0}Fe_{0.50}Mn_{0.50}O_2$ and O3-$Na_{0.83}Mg_{0.33}Fe_{0.17}Mn_{0.50}O_2$ determined from Rietveld refinement of its X-ray diffraction pattern.

O3-$Na_{1.0}Fe_{0.50}Mn_{0.50}O_2$						
Space group = R -3 m	R_{wp}=10.1 %	χ^2=1.65				
a = 2.94469(10) Å	b = 2.94469(10)Å	c =16.57300(58)Å				
Atom	Wyckoff position	x	y	z	occupancy	Biso
Na	3a	0	0	0	0.829(8)	1.03(1)
Fe	3b	0	0	0.5	0.504	1.20(8)
Mn	3b	0	0	0.5	0.504	1.20(8)
O	6c	0	0	0.23075(12)	1.014(3)	1.83(1)
O3-$Na_{0.83}Mg_{0.33}Fe_{0.17}Mn_{0.50}O_2$						
Space group = R -3 m	R_{wp}=11.7 %	χ^2=1.60				
a = 2.94562(4) Å	b =2.94562(4) Å	c =16.30951(38) Å				
Atom	Wyckoff position	x	y	z	occupancy	Biso
Na	3a	0	0	0	0.827(8)	1.45(8)
Mg	3b	0	0	0.5	0.332(7)	1.82(3)
Fe	3b	0	0	0.5	0.166(2)	1.82(3)
Mn	3b	0	0	0.5	0.544(2)	1.82(3)
O	6c	0	0	0.22933(12)	1.003(8)	1.42(6)

Table S3. Crystallographic data and atomic positions of the O3-$Na_{0.83}Mg_{0.33}Fe_{0.17}Mn_{0.50}O_2$ determined from Rietveld refinement of its neutron diffraction pattern.

NPD refinement results

Space group = R -3 m R_{wp}=2.986%

a = 2.94337(16) Å b = 2.94337(16) Å c = 16.3047(9) Å V = 122.330(6) Å^3

Atom	Wyckoff position	x	y	z	frac	Uiso
Na	3a	0	0	0	0.829(8)	0.0315
Mg	3b	0	0	0.5	0.333(2)	0.0172(8)
Fe	3b	0	0	0.5	0.166(6)	0.0172(8)
Mn	3b	0	0	0.5	0.500	0.0172(8)
O	6c	0	0	0.2305(1)	1.035(3)	0.0134(4)

nPDF refinement results

Space group = R -3 m R_w=25.266%

a = 2.951(1) Å b = 2.951 (1) Å c = 16.3574(94) Å

Atom	Wyckoff position	x	y	z	frac	Uiso
Na	3a	0	0	0	0.827(8)	0.0238(17)
Mg	3b	0	0	0.5	0.332(7)	0.0222(29)
Fe	3b	0	0	0.5	0.166(2)	0.0222(29)
Mn	3b	0	0	0.5	0.544(2)	0.0222(29)
O	6c	0	0	0.2310(5)	1.003(8)	0.014843(44)

Table S4. Comparison of electrochemical behaviors of various Na-ion half batteries.

Cathode	Voltage window (V)	Current density (mA g^{-1})	Average Voltage (V)	Capacity (mA h g^{-1})	Energy density (W h kg^{-1})	Ref.
$Na_{2/3}Fe_{1/2}Mn_{1/2}O_2$	1.5-4.3	12	2.6	184	478.4	1
$Na_{2/3}Fe_{2/3}Mn_{1/3}O_2$	1.5-4.2	0.1	2.6	190	497.8	2
$Na_{2/3}Fe_{1/3}Mn_{2/3}O_2$	1.5-4.8	0.1	2.7	157.5	429.9	3
$NaFe_{0.5}Co_{0.5}O_2$	2.5-4.0	12	2.2	120	264	4
$NaFe_{0.2}Mn_{0.4}Ni_{0.4}O_2$	2.0-4.0	12	3.1	160	502.4	5
$Na_xNi_{1/3}Fe_{1/3}Mn_{1/3}O_2$	2.0-4.3	~13	2.7	125	337.5	6
$Na_{0.9}Fe_{0.5}Mn_{0.5}O_2$	2.0-4.4	C/10	3.2	142.4	455.7	7
$Na_{45/54}Li_{4/54}Ni_{16/54}Mn_{34/54}O_2$	2.0-4.0	22	2.6	160	416	8
$NaNi_{0.4}Cu_{0.1}Mn_{0.4}Ti_{0.1}O_2$	2.4-4.5	C/10	3.2	102.5	328	9
$NaMnO_2$	2.0-3.8	24	3.2	171	547.2	10
$Na_{0.44}MnO_2$	2.0-4.0	12	2.7	185	499.5	11
$NaNi_{1/2}Mn_{1/2}O_2$	2.2-4.5	4.8	2.8	112	313.6	12
$Na_{2/3}Ni_{1/3}Mn_{2/3}O_2$	2.0-4.5	5	3.2	185	592	13
$Na_{0.9}Cu_{0.22}Fe_{0.30}Mn_{0.48}O_2$	2.5-4.05	10	3.6	161	579.6	14
$Na_{2/3}Mg_{0.28}Mn_{0.72}O_2$	2.0-4.5	10	2.6	210	546	15
$Na_{0.72}Li_{0.24}Mn_{0.76}O_2$	1.5-4.5	10	2.58	270	696.6	16
$NaFe_{0.5}Mn_{0.5}O_2$	1.5-4.3	10	2.6	184	478.4	This work
$Na_{0.83}Mg_{0.33}Fe_{0.17}Mn_{0.50}O_2$	**1.5-4.3**	**10**	**2.7**	**225**	**607.5**	**This work**

Table S5. Raw materials price ($ kg^{-1}) between January 2022 and September 2022

	Jan	Feb	Mar	Apl	Jun	May	Jul	Aug	Sept	Average
Na_2CO_3	0.37	0.36	0.38	0.40	0.40	0.41	0.41	0.42	0.39	0.39
MgO	0.16	0.23	0.23	0.25	0.22	0.21	0.19	0.19	0.16	0.21
Fe_2O_3	1.09	1.01	1.11	1.06	1.09	1.11	1.15	1.17	1.09	1.10
MnO_2	1.88	2.23	2.29	2.41	2.64	2.75	2.62	2.56	2.67	2.45

The data was collected from the website of the General Administration of Customs of the People's Republic of China. The data used to calculate the energy costs were based on the average price between January 2022 and September 2022.

Supplementary references

[1] N. Yabuuchi, M. Kajiyama, J. Iwatate, H. Nishikawa, S. Hitomi, R. Okuyama, R. Usui, Y. Yamada, S. Komaba, *Nat. Mater.* **2012**, *11*, 512.

[2] E. Gonzalo, M. H. Han, J. M. López del Amo, B. Acebedo, M. Casas-Cabanas, T. Rojo, *J. Mater. Chem. A* **2014**, *2*, 18523.

[3] T. KODERA, T. OGIHARA, *J. Ceram. Soc. Japan* **2014**, *122*, 483.

[4] H. Yoshida, N. Yabuuchi, S. Komaba, *Electrochem. commun.* **2013**, *34*, 60.

[5] D. D. Yuan, Y. X. Wang, Y. L. Cao, X. P. Ai, H. X. Yang, *ACS Appl. Mater. Interfaces* **2015**, *7*, 8585.

[6] Y. Xie, G.-L. Xu, H. Che, H. Wang, K. Yang, X. Yang, F. Guo, Y. Ren, Z. Chen, K. Amine, Z.-F. Ma, *Chem. Mater.* **2018**, *30*, 4909.

[7] A. Tripathi, S. Xi, S. R. Gajjela, P. Balaya, *Chem. Commun.* **2020**, *56*, 10686.

[8] C. Zhao, Z. Yao, Q. Wang, H. Li, J. Wang, M. Liu, S. Ganapathy, Y. Lu, J. Cabana, B. Li, X. Bai, A. Aspuru-Guzik, M. Wagemaker, L. Chen, Y.-S. Hu, *J. Am. Chem. Soc.* **2020**, *142*, 5742.

[9] Q. Wang, S. Mariyappan, J. Vergnet, A. M. Abakumov, G. Rousse, F. Rabuel, M. Chakir, J. M. Tarascon, *Adv. Energy Mater.* **2019**, *9*, 1.

[10] X. Ma, H. Chen, G. Ceder, *J. Electrochem. Soc.* **2011**, *158*, A1307.

[11] X. He, J. Wang, B. Qiu, E. Paillard, C. Ma, X. Cao, H. Liu, M. C. Stan, H. Liu, T. Gallash, Y. S. Meng, J. Li, *Nano Energy* **2016**, *27*, 602.

[12] S. Komaba, T. Nakayama, A. Ogata, T. Shimizu, C. Takei, S. Takada, A. Hokura, I. Nakai, *ECS Trans.* **2009**, *16*, 43.

[13] Z. Lu, J. R. Dahn, *J. Electrochem. Soc.* **2001**, *148*, A1225.

[14] L. Mu, S. Xu, Y. Li, Y. S. Hu, H. Li, L. Chen, X. Huang, *Adv. Mater.* **2015**, *27*, 6928.

[15] U. Maitra, R. A. House, J. W. Somerville, N. Tapia-Ruiz, J. G. Lozano, N. Guerrini, R. Hao, K. Luo, L. Jin, M. A. Pérez-Osorio, F. Massel, D. M. Pickup, S. Ramos, X. Lu, D. E. McNally, A. V. Chadwick, F. Giustino, T. Schmitt, L. C. Duda, M. R. Roberts, P. G. Bruce, *Nat. Chem.* **2018**, *10*, 288.

[16] X. Rong, E. Hu, Y. Lu, F. Meng, C. Zhao, X. Wang, Q. Zhang, X. Yu, L. Gu, Y. S. Hu, H. Li, X. Huang, X. Q. Yang, C. Delmas, L. Chen, *Joule* **2019**, *3*, 503.